Electron quantum path interferences in strongly laser driven aligned molecules and generation of circularly polarized XUVpulses.

PhD thesis by

Chatziathanasiou Stefanos

Heraklion, 2019

Electron quantum path interferences in strongly laser driven aligned molecules and generation of circularly polarized XUV pulses.

Submitted as doctoral thesis to the
Faculty of Physics of the university of Crete
Heraklion, Crete, Greece

Presented by
Chatziathanasiou Stefanos

Supervisors
Dr. Paraskevas Tzallas
Pr. Charalambidis Dimitrios

Επιβλέποντες
Τζάλλας Παρασκευάς
Χαραλαμπίδης Δημήτριος

Heraklion 2019
Ηράκλειο, 2019

List of publications in the course of this thesis

Polarization shaping of high order harmonics in laser aligned molecules
E. Skantzakis, **S. Chatziathanasiou**, P.A Carpeggiani, G. Sansone, A.Nayak, D. Gray, P. Tzallas, D. Charalambidis, E. Hertz and O. Faucher, Scientific Reports **6,** 39325 (2016).

Generation of Attosecond Light Pulses from Gas and Solid State Media
S. Chatziathanasiou, S. Kahaly, E. Skantzakis, G. Sansone, R. Lopez-Martens, S. Haessler, K. Varju, G.D. Tsakiris, D. Charalambidis and P. Tzallas, Photonics **4,** 26 (2017).

Time gated ion microscopy of light atom interactions
P. Tzallas, B. Bergues, D. Rompotis, N. Tsatrafyllis, **S. Chatziathanasiou**, A. Muschet, L. Veisz, H. Scroeder and D. Charalambidis, Journal of Optics **20,** 024018, (2018).

Imaging the source of high-harmonics generated in atomic gas media
S. Chatziathanasiou, S. Kahaly, D Charalambidis, P. Tzallas and E. Skantzakis, Opt. Express 27, 9733 (2019).

Quantum path interferences in high–harmonic generation from aligned diatomic molecules
S. Chatziathanasiou, I. Liontos, E. Skantzakis, S. Kahaly, M. Kahaly, N. Tsatrafyllis, O. Faucher,B. Witzel, N. Papadakis, D. Charalambidis and P. Tzallas (submitted)

Conference participations

Ultrafast dynamics with intense radiation sources
MEDEA summer school, Crete, Greece, October 2016.

The frontiers of attosecond and ultra-fast X-ray science
Erice, Sicily Italia, March 2017.

Ευχαριστίες

Η παρούσα διδακτορική διατριβή είναι αποτέλεσμα της συνεργασίας μιας ομάδας ανθρώπων τους οποίους θα ήθελα να ευχαριστήσω.

Αρχικά θα ήθελα να ευχαριστήσω ιδιαίτερα τον καθηγητή του Τμήματος Φυσικής του Πανεπιστημίου Κρήτης Δημήτρη Χαραλαμπίδη για την ευκαιρία που μου έδωσε να ασχοληθώ με τον τομέα της φυσικής ισχυρών πεδίων καθώς και για την γενικότερη επίβλεψη της διδακτορικής διατριβής.

Θα ήθελα να εκφράσω τις θερμότερες ευχαριστίες μου στον Δρ. Πάρη Τζάλλα, ερευνητή Α' του Ινστιτούτου Ηλεκτρονικής Δομής και Λέιζερ του Ιδρύματος Τεχνολογίας και Έρευνας για την επιστημονική καθοδήγηση καθ' όλη τη διάρκεια της εκπόνησης της παρούσας διατριβής. Ήταν δίπλα μου σε ότι τον χρειάστηκα τόσο σε επιστημονικό όσο και σε προσωπικό επίπεδο. Η επιτυχής ολοκλήρωση της διατριβής οφείλεται σε ένα μεγάλο ποσοστό σε αυτόν.

Στη συνέχεια θα ήθελα να ευχαριστήσω τον Δρ. Μανώλη Σκαντζάκη για την πολύτιμη βοήθεια του τόσο σε πειραματικό όσο και σε θεωρητικό επίπεδο από την πρώτη μέρα της παρουσίας μου στο εργαστήριο.

Επίσης θα ήθελα να ευχαριστήσω τα υπόλοιπα μέλη της ομάδας Δρ Νίκο Τσατραφύλλη , Δρ Νίκο Παπαδάκη και τους ΥΔ Ιωάννη Μάκο και Ιωάννη Ορφανό για την σημαντική τους βοήθεια και υποστήριξη.

Τέλος, θα ήθελα να ευχαριστήσω το ίδρυμα κρατικών υποτροφιών (ΙΚΥ) για την οικονομική βοήθεια που μου παρείχε. Η υλοποίηση της παρούσας διδακτορικής διατριβής συγχρηματοδοτήθηκε μέσω της Δράσης «ΕΝΙΣΧΥΣΗ ΤΟΥ ΑΝΘΡΩΠΙΝΟΥ ΕΡΕΥΝΗΤΙΚΟΥ ΔΥΝΑΜΙΚΟΥ ΜΕΣΩ ΤΗΣ ΥΛΟΠΟΙΗΣΗΣ ΔΙΔΑΚΤΟΡΙΚΗΣ ΕΡΕΥΝΑΣ» από πόρους του Επιχειρησιακού Προγράμματος «Ανάπτυξη Ανθρώπινου Δυναμικού, Εκπαίδευση και Δια Βίου Μάθηση», 2014-2020.

Χατζηαθανασίου Στέφανος

Σεπτέμβριος 2019

Contents

Περίληψη

Στην παρούσα διδακτορική διατριβή, χρησιμοποιώντας την απεικονιστική μέθοδο του μικροσκοπίου ιόντων χρονικής πύλης (Time Gated Ion Microscopy), μελετήθηκε η διαδικασία της παραγωγής των αρμονικών στην περιοχή της παραγωγής τους. Η μελέτη πραγματοποιήθηκε για αρμονικές που παράγονται από την αλληλεπίδραση ισχυρών IR παλμών λέιζερ με άτομα (Ar) και ευθυγραμμισμένα μόρια αζώτου (N_2). Η ευθυγράμμιση των μορίων επιτεύχθηκε με την ανάπτυξη μίας διάταξης άντλησης-ανίχνευσης (pump-probe). Η καταγραφή της χωρικής κατανομής της έντασης των αρμονικών στην περιοχή της παραγωγής τους οδήγησε σε σημαντικά συμπεράσματα τόσο για την εξάρτηση της διαδικασίας παραγωγής των αρμονικών από την σχετική θέση του jet παραγωγής και της δέσμης του IR στην περιοχή της παραγωγής των αρμονικών, όσο και για την δυναμική της ευθυγράμμισης των μορίων Η ίδια διάταξη χρησιμοποιήθηκε για την παραγωγή XUV ακτινοβολίας με υψηλό βαθμό ελλειπτικότητας από ευθυγραμμισμένα μόρια διοξειδίου του άνθρακα (CO_2).

Abstract

The aim of the thesis is to unravel the dynamics of the High Harmonic Generation (HHG) process induced in strongly laser driven aligned molecules and develop a method for the production of circularly polarized ultrashort pulses in the extreme-ultraviolet (XUV) spectral range. Towards these goals we have used the Time Gated Ion Microscopy (IM) technique and a pump-probe arrangement. The former maps the spatial XUV intensity distribution onto a spatial ion distribution (produced in the XUV focal area through a single–XUV– photon ionization process of an atomic gas). The pump–probe arrangement was used to trigger the molecular alignment process and generate the high–harmonics. Initially, in order to calibrate the harmonic generation/detection scheme, we have used only the IM and Argon atoms for the generation of high-harmonics. In this experiment we have measured and quantified the influence of spatiotemporal coupling effects in HHG region. After, using the IM approach in combination with the pump-probe arrangement, we have spatially resolved the interference pattern produced by the spatiotemporal overlap of the harmonics emitted by the short– and long–electron quantum paths, and we have succeeded in measuring in-situ their phase difference and disclose their dependence on molecular alignment. The findings constitute a vital step towards understanding of strong-field molecular physics and the development of a self-referenced attosecond spectroscopy approach. Additionally using the same pump-probe arrangement we demonstrate a method for the generation of circularly polarized XUV radiation a matter which is important for investigating phenomena such as circular dichroism, ultrafast spin dynamics, magnetic microscopy, chirality assignment e.t.c.

Introduction

HHG is a non-linear process in which harmonics are produced by the interaction of an intense IR laser pulse with an atomic or molecular medium. HHG provides a coherent radiation source in the extreme ultraviolet and soft x-ray regions of the spectrum and has the advantage to be feasible utilizing table top systems as opposed to large free electron laser systems (FEL). The HHG process itself can act as a probe of molecular structure and dynamics[1,2]. In addition, with the possibility of generating very short pulses of duration of the order of tens of attoseconds, i.e., the natural time scale of atomic physics, HHG sources are very useful in a wide range of practical applications such as time-resolved studies of ultrafast electronic dynamics[3].

The phenomenon was first observed in 1987 by McPherson et al. who successfully generated harmonic emission up to the 17th order at 248 nm in neon gas[4]. HHG can be understood through a three step semi-classical model (Corcum[5], Lewenstein et al[6]). According to this model, the laser field ionizes an atom or molecule (step1). The electron propagates to the continuum (step2) and when the laser field reverses direction it may return to the parent ion (step3) releasing its energy in the form of XUV photons.

Soon after the first observation of HHG from atoms the idea of using molecules as a generating medium came up. Over the last decade, HHG from field–free aligned molecules has attracted a keen interest from the scientific community as an important tool offering access to attosecond molecular spectroscopy and the ability of controlling the properties of the harmonics emitted in the extreme–ultraviolet (XUV)[1,2,7-15]. Linear molecules[16] are the most commonly used molecules in such studies which usually are investigated with a pump-probe arrangement. The main quest in the majority of these investigations is the connection of the properties of the emitted harmonics with the molecular structure. Towards this direction semiclassical theories (based on the electron recollision picture) and advanced mathematical algorithms, have been combined with sophisticated experimental methods and calibration approaches[7] aiming to obtain the dependence of the amplitude and phase of the emitted harmonics on the structure of the molecular orbital. The latter relies on the implementation of approaches like two–color (infrared (IR) and XUV) cross correlation[17,18], transient molecular grating[19-21], schemes based on two spatially separated XUV–sources[22-24] and gas mixtures[25-28]. However, a weakness in the majority of the demonstrated experimental approaches is the use of auxiliary references relaying on the assumption that they have similar response to strong field as the molecule under investigation[7]. This bottlenecks their applicability for revealing the dynamical information in a more versatile way and limits the accuracy of the measurements. Recent theoretical calculations have shown that a way to overcome this obstacle and purify the results, is to develop a self–referenced method relying on the use of the two–quantum path (Short (S) and Long (L)) interferences[29]. However, quantum path interferences were never observed experimentally in a molecular systems and hence their applicability on molecular attosecond spectroscopy remained an open question.

In the present thesis, by utilizing a pump-probe arrangement in combination with time gated Ion-Microscopy (I-M) after measuring the spatiotemporal coupling effects taking place in the HHG region we have developed a self-referenced approach that reveals the existence of quantum-path interference effects in laser-driven align molecules and we measure their dependence in molecular orientation without the use of an auxiliary atomic reference. Also, using the same pump-probe configuration we demonstrate a new method for the generation of circularly polarized XUV pulses based on aligned molecules as a generating medium.

The work is organized as follows: Chapter 1 describes the theory of HHG from atoms/molecules and the theory of molecular alignment. Chapter 2 begins with a short description of the operation principles of the I-M and continues with the experimental study regarding the dependence of the properties of the emitted XUV radiation on the focusing geometry. In chapter 3, the self-reference approach associated with the dynamics of high-harmonic generation from aligned molecules is demonstrated while chapter 4 deals with the new scheme which has been developed towards circularly polarized HHG from aligned molecules.

Chapter 1

Theory of HHG in atoms and molecules

The following chapter gives an overview of HHG from aligned linear molecules. Section 1.1 begins with the description of the HHG in atoms with a brief introduction to the semiclassical 3-step model. In the section 1.2 the dependence of the HHG process on the molecular orientation is presented in the framework of the three step model. Emphasis is given in the dependence of the third step of the model, the recollision process, on the molecular alignment. This dependence can provide information about molecular structure and dynamics. Section 1.3 describes the mechanism of the non-adiabatic (NAMA) molecular alignment from intense laser fields together with the parameters that can optimize the quality of the alignment. Finally, in section 1.4 the generation of harmonics with elliptical polarization using aligned molecules is presented.

1.1 High Harmonic Generation in atoms

HHG arise from the interaction of an intense laser field with atoms and was first observed by McPherson et al. in 1987[4] using a UV laser field and soon after by Ferray et al[30] using an IR laser field. Briefly, by focusing an intense ($I_L = 10^{14} - 10^{15}\ W/cm^2$) linearly polarized IR fs pulse to a cloud of atoms, an XUV frequency comb which consist odd harmonics of the driving frequency, is emitted in the direction of the laser field (figure 1.a). Due to the non-linearity of the harmonic generation process the divergence of the XUV beam is smaller compared to the IR driving field. The harmonic spectrum presents a characteristic behavior: After a rapid decrease in the first harmonic orders (which are generated by below the ionization threshold by multiphoton transitions in the perturbative regime), the harmonic conversion efficiency remains constant up to high order harmonics (this region of the spectrum is called plateau) and then drops rapidly in the cut-off region. Having the appropriate phase matching conditions (atomic response and macroscopic response) for the phase locking between the harmonics and selecting (using a bandpass thin metal filter) a group of harmonics blocking at the same time the fundamental pulse, an attosecond pulse train is formed with the individual pulses in the train to be separated by half of the laser period. The cut –off energy depends on the ionization potential I_p of the atom/molecule, the wavelength and the intensity of the driving field.

HHG can be described theoretically using the classical (where the laser field and electron are treated classically) and semi-classical (where the laser field is treated classically and the atom/electron

quantum mechanically) three step model. Although an accurate description of the HHG process requires the consideration of the laser bandwidth and the propagation effects in the medium, the fundamental properties of the interaction can be adequately explored with the single-color single-atom interaction. According to the classical approach of the three-step model (down panel of figure 1.1.b) introduced by Corkum[5], the electron tunnels out from the atomic/molecular potential distorted by the laser field, then accelerates in the laser field from which it gains kinetic energy and then it may recollide with the parent ion leading to the emission of extreme ultraviolet (EUV) light or soft x-rays (upper panel of 1b). As the recollision process takes place every half cycle of the driving field the resulting XUV spectrum consists of only odd harmonics of the fundamental (see blue filled area figure 1.1.c). The spectrum depicts a *plateau* region (where the XUV yield is approximately constant) which is extended up to a region that the yield drops rapidly called *cut-off* region where the energy of the emitted XUV photon is $\hbar\omega = I_p + 3.17U_p$ (U_pIs the ponteromotive energy of the electron). The electrons that are not recolliding with the ion or recollide elastically are contributing to the ATI spectrum.

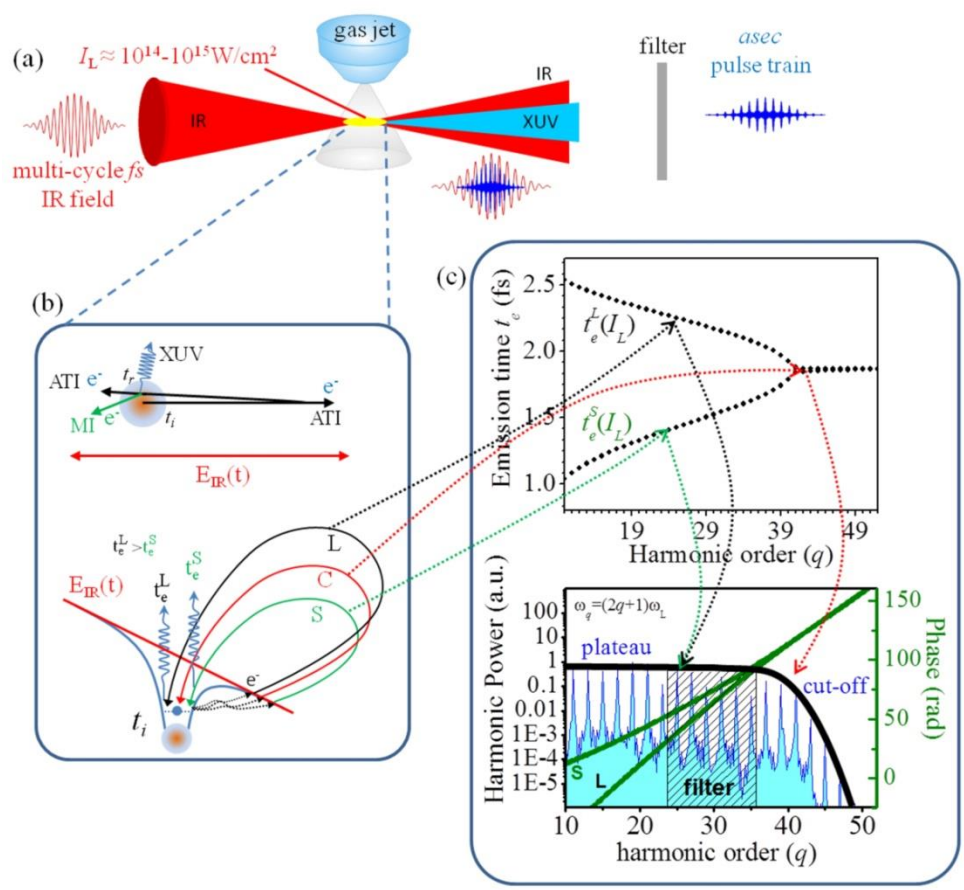

Figure 1.1: (a) A schematic representation of HHG in a gas phase media; (b) (upper panel) An oversimplified picture of the recollision process. The red arrow shows the polarization direction of the laser

field. t_i, t_r, MI, XUV, ATI are the ionization time, recombination time, multiple ionization ,generation of XUV radiation and above threshold ionization respectively; (down panel) HHG process in the spirit of three step model. L (black line) & S (green line) show the "long" and "short" electron trajectories contributing to the plateau harmonic emission while C (red line) shows the electron trajectory that contributes to the cut off harmonic emission; (c) (upper panel) Emission times as a function of the harmonic order q (calculated using the semi-classical 3-step model for $I_L = 10^{14}\ W/cm^2, I_P = 15eV$ and $\lambda = 800nm$). $t_e^L(I_L)$ & $t_e^S(I_L)$ depict the emission times (which depend on I_L) corresponding to the "long" and "short" electron trajectories. In the spirit of semi-classical 3-step model the emission times is the real part of the recombination time t_r; (down panel) Calculated harmonic spectrum (blue filled area) with $\omega_q = (2q+1)\omega_0$ (where ω_0 is the frequency of the IR field). The "Long" and "Short" trajectory harmonics, which contribute in plateau region, degenerate to a single trajectory in the cut-off region of the spectrum. The green solid line is the spectral phase distribution of the S and L trajectory harmonics. The black solid line illustrates the XUV continuum spectrum emitted in case of a single electron recollision. The line-shaded area illustrates the bandwidth of the XUV radiation which passes through a band pass XUV filter.

Lewenstein[6] presented a semi-classical version of the classical model which includes important quantum-mechanical effects such as quantum interferences giving a deeper physical understanding of the HHG process. In this context the harmonic spectrum is obtained by the Fourier transform of the time-dependent dipole moment which contains an integral over all possible electron trajectories characterized by an ionization time (t_i), a recombination time (t_r) and momentum p.

The time-dependent Shröedinger equation (TDSE) for an atom under the influence of a laser field can be expressed as:

$$i\frac{\partial}{\partial t}|\psi(r,t)\rangle = [-\frac{1}{2}\nabla^2 + V(r) - E(t)\cdot r]|\psi(r,t)\rangle \tag{1.1}$$

where $V(r)$ is the atomic potential and $E(t)$ is the electric field of the laser. Two approximations are made in the three step model. The single active electron (SAE) approximation and the strong field approximation (SFA). The latter is using the following three assumptions:

1. Only the ground bound state is considered.
2. The depletion of the ground bound state can be neglected.
3. In the continuum the electron can be treated as a "free" particle, with no effect of the atomic potential.

After making the above three approximations the time-dependent wavefunction of the electron can be expanded as:

$$|\psi(r,t)\rangle = e^{iI_p(t)}(a(t)|0\rangle + \int \frac{d^3k}{2\pi^3} b(k,t)e^{ikr}) \tag{1.2}$$

where $a(t) \approx 1$ is the ground state amplitude and $b(k,t)$ are the amplitudes of continuum states with momentum $|k\rangle$ written here as superposition of plane waves.

After solving the Schrödinger equation for the amplitudes $b(k,t)$ the time-dependent dipole can be obtained from:

$$r(t) = \langle \psi(r,t)|r|\psi(r,t)\rangle \tag{1.3}$$

Neglecting the contributions from continuum-continuum transitions and the depletion of the ground state by setting $a(t) = 1$ we get the final expression of the dipole moment:

$$r(t) = i\int_0^t dt' \int d^3\,\vec{p}\;\; d^*{}_{\vec{p}-\vec{A}(t_r)}\, e^{iS(p,t_i,t_r)}\, E(t_i)\cdot d_{\vec{p}-\vec{A}(t_i)} + c.c \tag{1.4}$$

where S is the quasiclassical action that the electron requires during its excursion to the laser field :

$$S(\vec{p},t,t') = \int_{t_i'}^{t_r} dt''\left(\frac{(\vec{p}-\vec{A}(t''))^2}{2} + I_p\right) \tag{1.5}$$

In the above equations we have introduced the canonical momentum $\vec{p}$:

$$\vec{\vec{k}} = p - \vec{A}(t) \tag{1.6}$$

and the vector potential of the electric field $\vec{A}(t)$:

$$E(t) = -\frac{\partial A(t)}{\partial t} \tag{1.7}$$

Equation 1.4 contains the three steps of the semi-classical approach: At time t_i the electrons tunnels from the ground state $|0\rangle$ into the continuum with canonical momentum $\vec{p}$ (step1). The probability amplitude for the transition is given by $E(t_i)\cdot d_{\vec{p}-\vec{A}(t_i)}$, where $d_{\vec{p}-\vec{A}(t_i)} = \langle \vec{p}-\vec{A}(t_i)|r|0\rangle$ is the dipole matrix element. At the continuum the electron wavepacket propagates under the influence of the laser field only and acquires phase factor equal to $e^{iS(p,t_i,t_r)}$ (step2). Finally, the electron recombines with the core at time t_r. The recombination matrix element is $d^*{}_{\vec{p}-\vec{A}(t_r)} = \langle 0|r|\vec{p}-\vec{A}(t_r)\rangle$.The harmonic spectra for a single atom is obtained from the Fourier transformation of the dipole moment $r(t)$:

$$r(\omega) = F_{t\to\omega}\left[\frac{d^2}{dt^2}\langle \psi(r,t)|r|\psi(r,t)\rangle\right] = -\omega^2 F_{t\to\omega}[\langle \psi(r,t)|r|\psi(r,t)\rangle] \tag{1.8}$$

Using a saddle-point approximation it can be shown that for a given laser intensity I_L there are two interfering electron trajectories for the harmonics in the *plateau* region[31-34] dominating the emission of a given harmonic order q in the plateau region of the spectrum. Depending on the time τ spent in the continuum these trajectories called *Short* (S) and *Long (L)* ($\tau_q^L > \tau_q^S$). For the *Long* trajectories $\tau_q^L = t_r^L - t_i^L \approx T_L$ while for the short $\tau_q^S = t_r^S - t_i^S \approx T_L/2$, where T_L is the laser cycle period). The two trajectories degenerate into a single one for the harmonics laying in the *cut-off* region (noted as C in the down panel of figure 1). The phase of each harmonic order q results from the phase accumulated by the electron trajectory in the continuum (which can be approximate by $\approx -\tau_q^{L,S}U_p$) and the phase ($\omega_q t_r$) introduced by the recombination time measured with respect to the reference time of the laser period (upper panel of figure 1c) i.e $\varphi_q^{S,L} = \omega_q t_r^{S,L} + \tau_q^{L,S}U_p$. The green solid line in the down panel of figure 1c shows the harmonic

spectral phase distribution calculated using the semi-classical 3-step model. Due to the lack of synchronization during the generation process the harmonics have an inherent linear chirp (which is positive for the short S and negative for the long L trajectories).

1.1.1 Macroscopic effects in the HHG

In a real experiment the XUV signal results from the superposition of the elementary contributions from the single atoms/molecules emitting XUV photons on the focus of the IR laser beam. It is well known in linear optics that the generation of new frequency components is effective only if the phase velocity of the fundamental field (in the case of HHG usually the IR laser) and that of the generated (the XUV field) can be matched over the length of the generated medium. For the HHG, the contributions that cause a wavevector phase mismatch Δk_q between the fundamental and the qth harmonic along the medium length are:

- Gouy phase shift, δk_g — affects the focused Gaussian IR beam, there is a negative contribution as we go from before focus to after focus. The phase shift through the focus (from the far field to the far field on the other side of the focus) is π.
- Dipole phase, δk_d — is proportional to the intensity of the IR field, and depends on whether the generation occurs via the short or long trajectory. As the driving field intensity is space and time dependent, this component also varies spatiotemporally.
- Dispersion of the neutral atoms, δk_a — for the XUV spectral domain it is negative, for IR components it is positive.
- Plasma dispersion, δk_p — it is always negative and scales with λ^2 so IR is affected more by it. Since ionization fraction varies in space and time, this contribution is also varying.

Therefore the total wavevector phase mismatch can be expressed as

$$\Delta k_q = \delta k_g + \delta k_d + \delta k_a + \delta k_p \tag{1.9}$$

Harmonic generation is optimized when the phase mismatch is minimized along the medium length is minimized, i.e when $\Delta k_q \to 0$.

1.2 Semi-classical description of HHG process in molecules

The semi-classical approach of the three step model for atoms described in section 1.1 has been extended to molecules by Zhou et. al [35] in 2005. The same approximations based on the SFA ans SAE made for the atomic case are valid for molecules as well. The molecular harmonic spectra is obtained the Fourier transform of the time-dependent dipole moment $r_m(t)$. For the calculation of the dipole moment for molecules the laser polarization and the molecular axis are chosen to be on the *y*-*z* plane, with the molecular

axis being along the z axis. The angle between the polarization direction of the laser and the molecular axis is θ. The time-dependent dipole moment for molecules under the saddle point approximation is[35]:

$$r_m(t) = i\int_0^{\infty} d\tau \left(\frac{\pi}{\epsilon+\frac{i\pi}{2}}\right)^{\frac{3}{2}} \{sin^2\theta d_y^*(t)d_y(t-\tau) + cos^2\theta d_z^*(t)d_z(t-\tau) + sin\theta cos\theta\left[d_y^*(t)d_z(t-\tau) + d_z^*(t)d_y(t-\tau)\right]\}e^{-iS_{st}(t,\tau)} + c.c \quad (1.10)$$

where d_y and d_z are the components of the dipole moment along y and z direction respectively. The components of the dipole moment are calculated using the ground bound state of molecule, highest occupied molecular orbital (HOMO). Using the linear combination of atomic orbitals method (LCAO) the HOMO bound state for a diatomic molecule can be expressed as:

$$\Psi_g^{\alpha}(r) \sim \Phi_0(r-R/2) - \Phi_0(r+R/2) \quad (1.11)$$

for an antisymmetric combination and

$$\Psi_g^{s}(r) \sim \Phi_0(r-R/2) + \Phi_0(r+R/2) \quad (1.12)$$

for a symmetric combination of atomic orbitals, where R is the internuclear distance and Φ_0 the atomic orbital. The transition matrix element between the molecular ground state and the plane wave –continuum state is now:

$$d_y^a \sim \langle \Psi_c | r | \Psi_g^{\alpha} \rangle \sim 2isin\left(\frac{k\cdot R}{2}\right) \langle e^{ikr} | r | \Phi_0 \rangle \quad (1.13)$$

and

$$d_y^s \sim \langle \Psi_c | r | \Psi_g^{s} \rangle \sim 2cos\left(\frac{k\cdot R}{2}\right) \langle e^{ikr} | r | \Phi_0 \rangle \quad (1.14)$$

respectively. Meanwhile, d_z has a similar expression. The above equations 1.13&1.14 reveal the difference between HHG from atoms and diatomic molecules. Compared with the atomic case, the transition amplitudes for molecular HHG depend on the molecular orientation with respect to the electron recollision direction, the internuclear distance R and the symmetry of the molecular orbital. The molecular harmonic spectra thus can provide information about the molecular structure.

High harmonics from a sample of randomly distributed molecules have characteristics similar to those of harmonics generated from atoms. The harmonic spectrum shows a clear plateau and cut off region like the atomic case in figure 1c (down). The situation is different for a sample of aligned linear molecules because the ionization/recombination rate and ionization/recombination times depend on the angle between the molecular orbital and the laser polarization[36].

Briefly, (details can be found in[37]) the tunneling ionization rate depends on the orientation of the electron density with respect with the laser polarization. The tunneling rate is larger when the electronic density is aligned with the laser field direction. For molecules with σ_g symmetry orbital like N_2 the electronic density is aligned along the molecular axis while for molecules with π_g symmetry like O_2 the

electronic density is aligned preferentially in a direction perpendicular to the molecular axis (figure 1.2). Thus for N_2 the ionization rate is enhanced if the molecular axis is aligned along the laser field direction while for O_2 is suppressed. According to the 3-step model, the tunneling ionization time depends on the angle between the molecular potential (or molecular orbital) and the laser polarization. As the properties (phase, amplitude) of the electron wave packet in the continuum (with a wavefunction Ψ_c) are directly associated with the ionization time t_i it is evident the different angles between the molecular axis and the laser polarization will result to an electron wavepacket with different Ψ_c in the continuum.

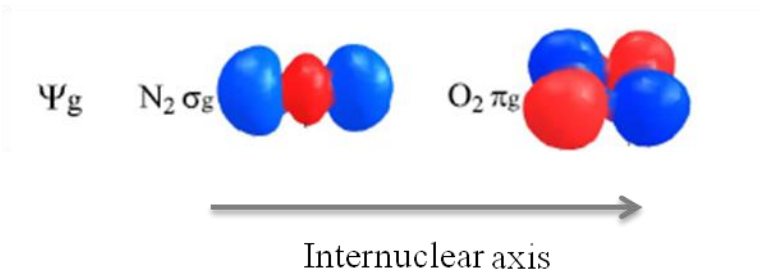

Figure 1.2: The electron density of the HOMO orbitals of N_2 and O_2. The internuclear axis is horizontal for both molecules [Figure taken from ref. 36].

The electron propagation in the continuum influences the recollision process as well. The recolliding electron wave packet Ψ_c (considered as a plane wave moving along the direction of the driving laser field polarization) overlaps the remaining part of the HOMO orbital wave function Ψ_g. The coherent addition of the two wavefunctions induces a dipole, $d_r(t) = \langle \Psi_c | r | \Psi_g \rangle$, that depends on the angle θ between the molecular axis and the driving field polarization, affecting the phase/amplitude of the emitted harmonics. For example, in N_2 when the HOMO spatial distribution (which is aligned along the molecular axis) is parallel ($\theta = 0°$) to the polarization of the driving laser field, the dipole $d_r(t)$ is strong and leads to enhanced harmonic emission compared to the case of N_2 molecules aligned perpendicularly ($\theta = 90°$) to the laser polarization[38]. When molecules with HOMO of π_g symmetry like O_2 are aligned parallel to the laser field ($\theta = 0°$) the induced dipole is weak and results to a harmonic emission which is reduced compared to $\theta = 45°$ where the two lobes of the HOMO orbital are parallel to the laser polarization (fig. 1.2 right panel) [36].

.

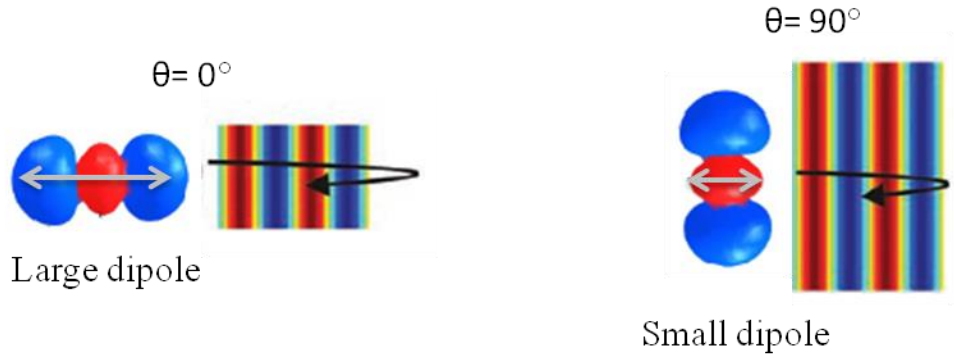

Figure 1.3 Sketch of the recollision wavepacket for a driving field polarized along the internuclear axis of N_2 (θ = 0°) and perpendicularly (θ = 90°). The induced dipole is strong leading to enhanced harmonic emission when the driving field is aligned along the molecular axis compared to the case of N_2 molecules aligned perpendicularly when the dipole is small [figure taken from ref. [38]].

The first indication that harmonic spectra from aligned molecules carry information about the molecular structure came from numerical simulations of the HHG from aligned H_2 and H_2[9,10] (figure 1.3). These simulations showed a very interesting feature in the harmonic spectra with a pronounced minimum in the plateau region. This feature was explained immediately through a two-center interference model focused on the recombination step. As already mentioned, in the recombination matrix element exist a sine function for an antisymmetric HOMO wavefunction (see equation 1.13). A destructive interference occurs when $\frac{kR}{2} = n\pi$, that is when

$$Rcos\theta = n\,\lambda \tag{1.15}$$

and constructive when

$$Rcos\theta = (2n+1)\frac{\lambda}{2} \tag{1.16}$$

where θ is the angle between the molecular axis and the electron recollision direction given by the laser polarization, λ is the De Broglie wavelength of the electron and n is an integer.

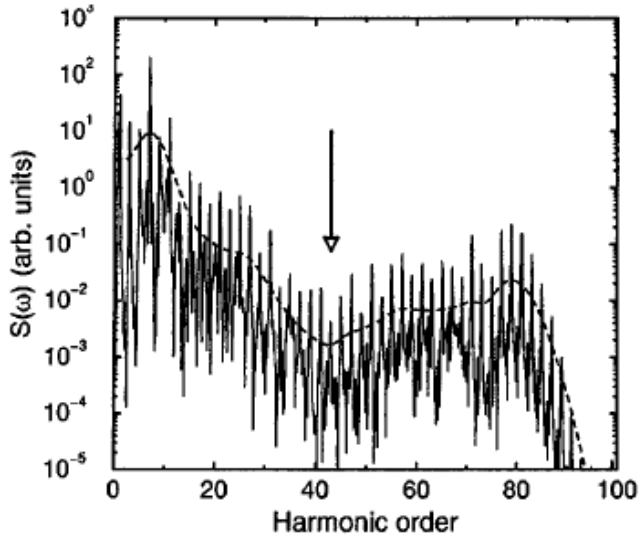

Figure 1.4: The harmonic spectra of H_2^+ calculated numerically with a clear minimum in the plateau region indicated by the arrow. The molecule is aligned at 40° with respect to the laser axis. Dashed line: Smoothed spectrum [figure from ref].

The molecule behaves as a two-point emitter with a phase difference between the two emitters (located at the two nuclei) determined from the de Broglie wavelength of the returning electron λ and the projection of the internuclear distance on the laser polarization direction, $Rcos\theta$ (figure 1.5). For a symmetric molecule the conditions for the equations 1.15 and 1.16 are reversed.

Experimentally two center interference was demonstrated few years later[1,11] in CO_2 molecule that can be regarded as an elongated diatomic molecule where the point emitters are located in the two O nuclei. The O-O distance in CO_2 is 4.39a.u that corresponds to an electron wavelength typical of the harmonic generation process. The electron de Broglie wavelength $\lambda = 2\pi/k$ is related with the energy of the emitted photon with the relation $E = \frac{\hbar^2 k^2}{2m_e}$. For θ = 0 the first destructive interference is expected at harmonic order q=19.

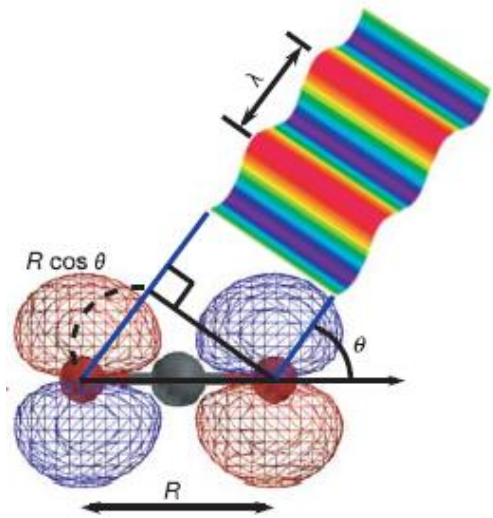

Figure 1.5: Schematic representation of the two center interference model for a CO_2 molecule. R is the distance between the two O atoms, θ is the orientation angle and λ is the de Broglie wavelength of the electron [Figure from ref.[1]].

Another approach to extract information for the molecular structure using HHG is the molecular-orbital tomography[7].This method takes advantage of the sensitivity of the HHG to the electron recombination process. As already discussed in section 1.1 the harmonic spectra $r(\omega)$ is obtained from the fourier transform of the time dependent dipole moment. The transition dipole moment in the spectral domain (in the plane wave approximation) is $r(\omega) = b(k) \int \Psi_g(r) r e^{ikx} dr$ where $b(k)$ is the electron wavepacket amplitude and the integral describes the recombination step. The harmonic intensity can be written as $S(\omega) \approx \omega^4 |r(\omega)|^2$. If $b(k)$ is known the experimental measurement of the harmonic spectra is an experimental determination of the integral $\int \Psi_g(r) r e^{ikx} dr$ that is the 1D spatial Fourier transform of the $r\Psi_g$ in the k direction. The plane wave amplitude $b(k)$ can be obtained independently by measuring the harmonic spectra of a reference atom with similar I_p with the molecule under investigation (for details see ref.[7]). By recording the harmonic spectrum from a sample of aligned molecules at various angles between the molecule and the electron recollision direction (k direction) and then apply an inverse Fourier transform at the obtained data the shape of the molecular orbital Ψ_g of can be reconstructed.

1.3 Laser induced molecular alignment

The interaction of a linear molecule with an intense laser field ($I = 10^{12} - 10^{13}\ W/cm^2$) leads to the alignment of the molecular axis along the polarization direction of the laser field. In a classical picture, the electric field $\vec{E}$ induces a molecular dipole $\vec{\mu} = a \cdot \vec{E}$ where a is the polarizability tensor, and interacts with it. The interaction energy is[39]:

$$H_{int} = -\frac{1}{4}E^2(\Delta\alpha cos^2\theta + \alpha \perp) \tag{1.17}$$

E is the envelope of the electric field, $\Delta\alpha$ the polarizability anisotropy $\alpha \perp$ the polarizability $a_\perp$ perpendicular to the molecular axis and θ the angle between the molecular axis and the polarization of the laser field. In linear molecules the polarizability along the molecular axis $a_\parallel$ is usually larger than the polarizability $a_\perp$ perpendicular to the molecular axis. Due to the anisotropy of the molecular polarizability the interaction of the induced dipole with the electric field induces a torque $\tau \propto -\Delta\alpha sin2\theta$[40] that tends to align the molecular axis along the laser polarization direction (see figure 1.6).

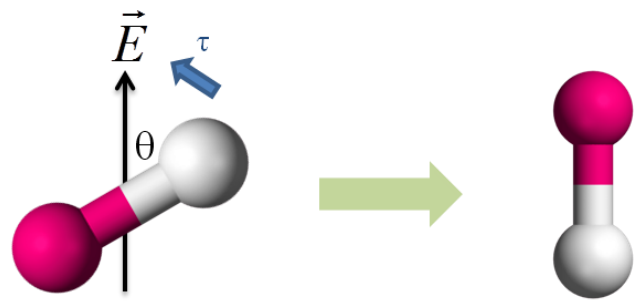

Figure 1.6. Schematic representation of a linear molecule interacting with a laser pulse with polarization along the vertical direction (black arrow). θ is the angle between the molecular axis and the polarization of the laser field. A torque τ (blue arrow) is exerted to the molecule due to the interaction of the laser pulse with the induced dipole leading to the alignment of the molecular axis along the laser pulse polarization direction (right panel).

In order to align the molecule the intensity of the laser field must be sufficient intense to rotate the molecules, but not intense enough to ionize/destroy the molecule. Furthermore, the interaction of the pulse with the molecules should be non-resonant in order to avoid any excitation of higher electronic/vibronic states.

There are two types of laser induced alignment: The *adiabatic* and the *non adiabatic* (NAMA) or *field free* molecular alignment. Adiabatic alignment occurs when the pulse duration is longer than the rotational period of the molecule,$\tau_{pulse} > T_{rot}$, (T_{rot} few ps for the linear molecules) . In this case, when the molecules interact with the pulse they adiabatically align themselves in the direction of the laser pulse. When the laser pulse is over, the molecular ensemble returns to the isotropic angular distribution. NAMA

occurs when the pulse duration is much shorter than the rotational period $\tau_{pulse} \ll T_{rot}$. In this case the molecules can be considered as 'frozen' while the laser pulse gives them a "kick" towards alignment. Quantum-mechanically the interaction with the non- resonant short laser pulse creates a coherent superposition of rotational states (lying on the ground electron state) through sequential Raman transitions[40,41,42](figure 1.7). The rotational wave packet evolves in time and periodically (at multiple times of its rotational period T_{rot}) rephases and dephases due to coherent superposition of the different rotational states.

A significant advantage of NAMA in comparison with the adiabatic alignment is that the molecule remains aligned even when the laser pulse is off. Thus, the NAMA has been used in the majority of the studies (including the work of the present thesis) concerning interactions with aligned molecules. Detailed description of NAMA dynamics is given in the next section.

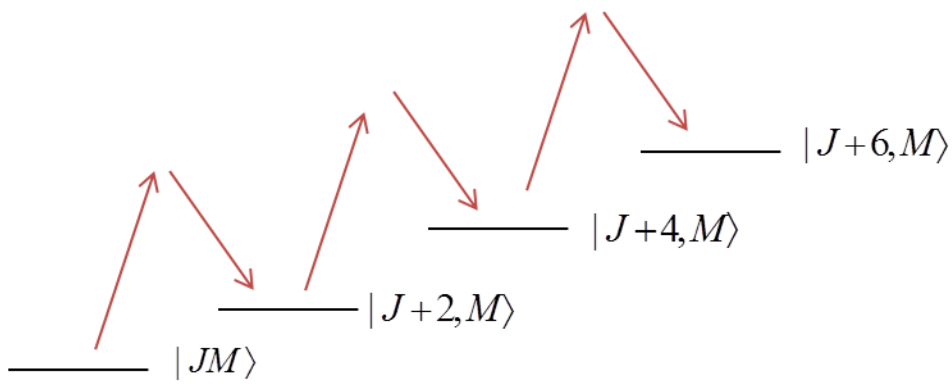

Figure 1.7: The creation of the rotational wavepacket through the sequential Raman transition. The selection rules for the transitions are $\Delta J = 0, \pm 2$ and $\Delta M = 0$.

1.3.1 Rotational wave packets dynamics

Quantum mechanically, the rotational wavepacket can be written as the sum over the molecular rotational states:

$$\Psi(t) = \sum_{J,M} c_{J,M} e^{-i(E_J/\hbar)t} |J, M\rangle \tag{1.18}$$

where $E_J = BJ(J+1)$ are the energy eigenvalues , $B = \hbar c B_0$ is the rotational constant of the molecules which determines the time-scale of the rotational dynamics and B_0 is the ground state rotational constant and $c_{J,M}$ the expansion coefficients. $|J\rangle$ is the quantum number for angular momentum and $|M\rangle$ its projection on the polarization axis of the aligning pulse. As indicated in the previous section the interaction of the aligning pulse with the molecule leads to a generation of a coherent rotational wave packet via sequential Raman transitions. The selection rules for Raman transitions are $\Delta J = 0, \pm 2$ and $\Delta M = 0$ for a linearly polarized pulse[40-42]. The rotational wavepacket accumulates energy dependent phase. If we consider a time

$t = \pi\hbar/B$ (that equals the rotational period of the molecules T_{rot}) the phase of each state is $\pi J(J+1)$. Since J is restricted to integer values the phase at this time is a multiple integer of 2π for all possible J states. This means that at time t (and multiple of this time) the wavepacket is reproduced again. This process is called a *wave packer revival*.

The degree of alignment is usually expressed by the expectation value of $cos^2\theta$, i.e $< cos^2\theta >= \langle \Psi(t)|cos^2\theta|\Psi(t)\rangle$ called *aligning parameter*. This quantity can be calculated by solving the time-dependent Shrödinger equation (TDSE):

$$i\hbar\frac{\partial\Psi(t)}{\partial t} = (H_{rot} + H_{int})\Psi(t) \tag{1.19}$$

where $H_{rot} = BJ^2$ is the rotational kinetic energy, $H_{int} = -\frac{1}{4}E^2(\Delta\alpha cos^2\theta + \alpha\perp)$ and $\Psi(t)$ is the rotational wavepacket. The initial condition is that the molecule is in a single rotational state $|J_i, M\rangle$. The aligning parameter is given by:

$$< cos^2\theta >= \langle \Psi(t)|cos^2\theta|\Psi(t)\rangle = \sum_{J',M'} \sum_{J,M} c^*_{J",M}\, c_{J,M} \langle J', M'|cos^2\theta|J, M\rangle\, e^{-\frac{i}{\hbar}(E_{J'}-E_J)t} \tag{1.20}$$

The observable of interest $cos^2\theta$ couples only J states with the same parity ($J' = J, J' = J \pm 2$). Since initially, the molecular ensemble is in a mixture of rotational states (incoherent ensemble) the TDSE must be calculated for every $|J_i, M\rangle$ present in the initial condition. The expectation value is then thermally averaged:

$$< cos^2\theta >= \sum_{J_i} w_{J_i} \sum_{J',M'} \sum_{J,M} c^*_{J",M}\, c_{J,M} \langle J', M'|cos^2\theta|J, M\rangle\, e^{-\frac{i}{\hbar}(E_{J'}-E_J)t} \tag{1.21}$$

where w_{J_i} stands for the initial population of state $|J_i, M\rangle$.

If the molecules are predominantly aligned along the polarization axis of the electric field $\langle cos^2\theta\rangle > 1/3$[43]. For an isotropic distribution oriented randomly across all θ, $\langle cos^2\theta\rangle = 1/3$ and for molecules aligned predominantly perpendicularly to the polarization axis of the field, i.e anti-aligned molecules $\langle cos^2\theta\rangle < 1/3$[43]. In the figure 1.8 the calculated time – dependent alignment parameter $\langle cos^2\theta\rangle$ of N_2 with $T_{rot} \sim 8.4$ ps and O_2 with with $T_{rot} \sim 11.7$ ps is presented. The theoretical calculations of the aligning parameter in this work have been done using Webber's code[44] that numerically calculates the evolution of $\Psi(t)$ using the fourth-order Runge-Kutta method[45]

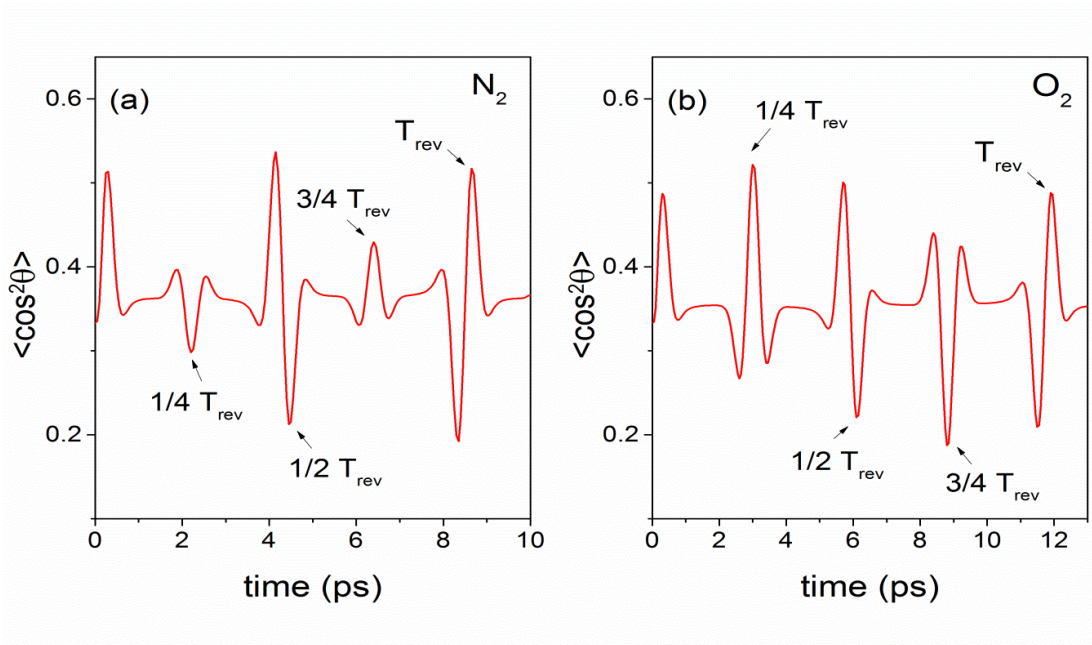

Figure 1.8: Theoretical calculation of the alignment parameter $\langle cos^2\theta \rangle$ calculated for a peak intensity of $2.3 \times 10^{13} W/cm^2$, pulse duration 100 fs and temperature 70 K, for N_2 (a) and O_2 (b). The calculation has been performed using the code of Sebastian Webber[44].

From the figure 1.8 is clear that significant alignment and anti-alignment occurs not only at the revival time T_{rev} but also at fractional revival times $t = nT_{rev}$, for $n = \frac{1}{4}, \frac{1}{2}, \frac{3}{4}$. For $J = J' \pm 2$ the phase term of equation 1.22 can be written as $\varphi(t) = \pi(4J + 6)t$. At full revival time, $t = 1$ and the phase $\varphi(t)$ is integer multiple of 2π for all J states as already discussed. At half-revival, $t = 1/2$ and $\varphi(t)$ is odd multiple of π for all J states. The wavepacket is π-shifted with respect with the full revival and the molecules are anti-aligned. However, at quarter revivals ($t = 1/4$ &$3/4$) even and odd J states interfere destructively since their contributions are π-shifted. The relative weights of the even and odd J states are determined from the nuclear spin statistics[46]. For N_2 the ratio of even to odd is 2:1 so the amplitude of the quarter revival is half of that of the full revival while in O_2, only odd J are present in the rotational wave packet and the signal is equal for all the revivals as illustrated in figure 1.8. In the case of the N_2O the quarter revivals are cancelled out because of the one to one ratio between even and odd J states. In the table below the relative weights for four molecules are presented.

	w_{even}	w_{odd}
N_2	2	1
O_2	0	1
CO_2	1	0
N_2O	1	1

Table 1.1: The relative weights of even and odd rotational states for various molecules.

The degree of alignment depends on the laser intensity, the pulse duration and the rotational temperature of the molecular ensemble. The role of the above parameters will be described in the following section.

1.3.2 Optimization of NAMA

Theoretical simulations using the code of Sebastian Webber allowed us to study extensively the dependence of molecular alignment on the experimental parameters (intensity, pulse duration, molecular temperature). Simulations have shown that the alignment is increasing with the intensity of the laser pulse. An intense laser pulse can couple more rotational states leading to a spectrally broad rotational wave packet and a high degree of alignment (figure 1.9a). However, there are limitations since a strong pulse can lead to undesirable side effects such as ionization of the molecules.

The degree of alignment depends also on the temperature of the molecules. Rotationally cold molecules enhance the degree of alignment as indicated in figure 1.9 b. Only the wavepackets created from one particular initial rotational state $|J_i M\rangle$ are coherent. For hot molecules the number of the incoherently excited initial rotational levels is increased giving rise to wavepackets without a definite phase relation between them, lowering the achievable degree of alignment[47]. Molecules can be cooled rotationally trough supersonic expansion into vacuum using a pulsed gas jet. The operation principle of the super-sonic jet will be described in the next section.

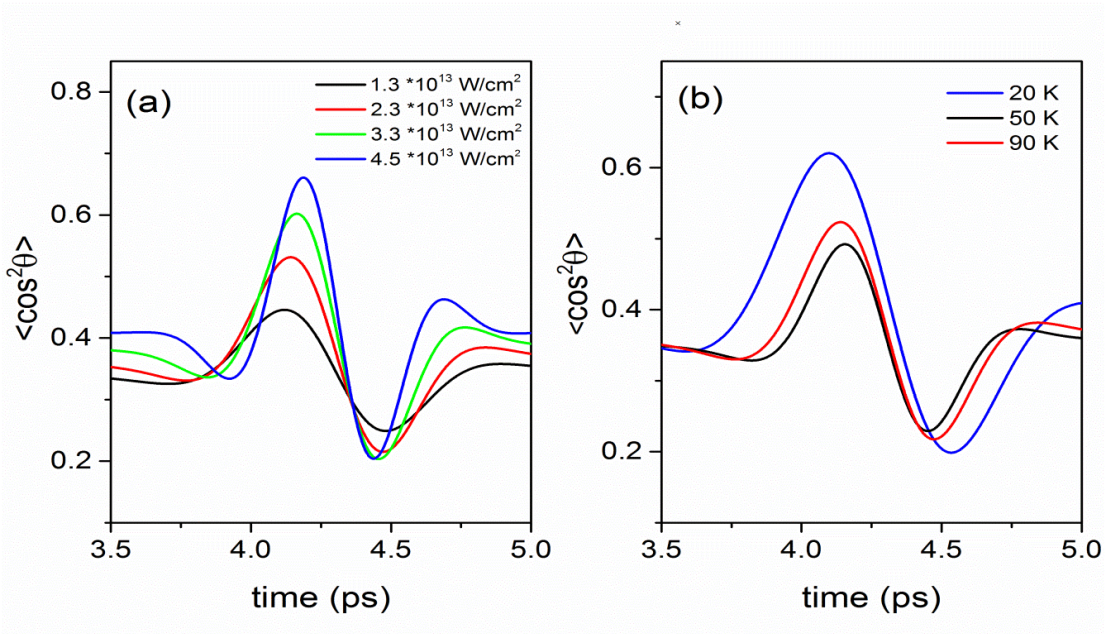

Figure 1.9: (a) The aligning parameter $\langle cos^2\theta \rangle$ of the $T_r/2$ revival of N_2 calculated for various intensities ranging from $2.3 \times 10^{13} W/cm^2$ to $4.5 \times 10^{13}\ W/cm^2$ with pulse duration 100 fs and temperature 70 K. (b) The aligning parameter $\langle cos^2\theta \rangle$ calculated for different temperatures with peak intensity of $2.3 \times 10^{13} W/cm^2$ and pulse duration 100 fs.

The dependence of the molecular alignment on the pulse duration is shown fig. 1.7. The pulse duration should be short compared to the molecular period T_{rot} in order for the molecule to be rotationally 'frozen' during the interaction. This way the interaction can be considered as a'kick' encoded in the wave packet's rotational composition giving rise to alignment after the pulse turn-off[41.] The general rule is that $\tau_{pulse} \ll T_{rot}$. However, keeping the intensity constant the pulse duration can be stretched in order to increase the energy content of the pulse. The alignment is enhanced in a similar way as increasing the intensity without the unwanted side effects. The pulse duration can be increased as long the process is non-adiabatic. For $\tau_{pulse} \geq 200$ fs the revival structure starts being distorted – the process is not anymore pure non adiabatic (figure 1.10 c) and for much longer pulse durations the adiabatic regime is dominating (figure 1.10 d). Finally, it has to be noted that molecules with a larger anisotropic polarizability are more easily aligned. For example, CO_2 can be aligned more strongly than N_2 under equivalent conditions.

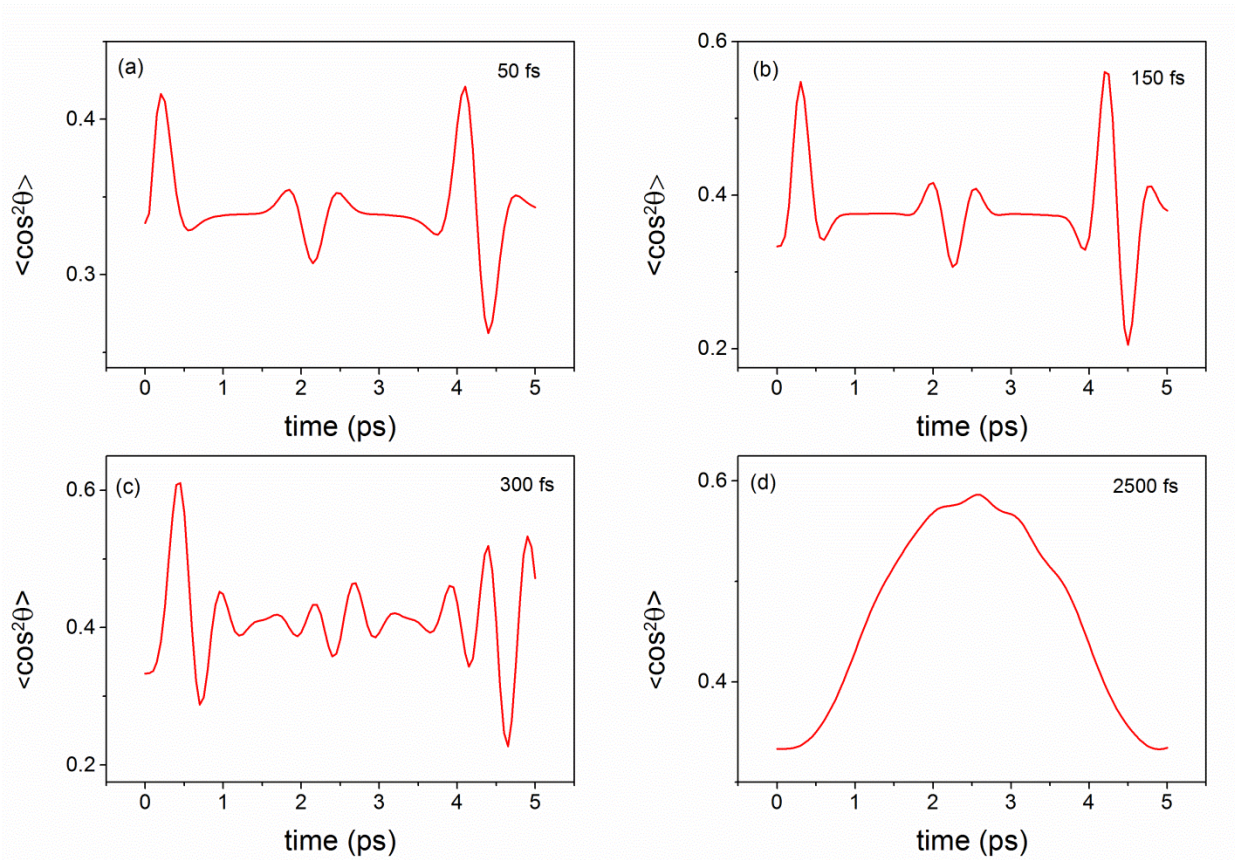

Figure 1.10: Dynamics of N_2 aligning parameter $\langle cos^2\theta \rangle$ for $T_r/2$ &$T_r/4$ revivals calculated for a peak intensity of $2.3 \times 10^{13} W/cm^2$ and temperature 70K for four different pulse durations.

1.3.3 Supersonic expansion

As explained in the section 1.3.2 the degree of alignment increases with cold rotational molecules. Low molecular temperatures can be achieved when a high pressure gas (usually ~ 3-5 bars of backing pressure) is injected through a small orifice (typically < 1mm diameter) into vacuum, forming a supersonic jet-expansion. The molecules undergo many collisions and the gas accelerates from the high pressure to the low pressure zone. The molecule during this process cools down, loosing most of its rotational and vibrational energy that is converted to directed translational energy. Very rapidly the molecular speeds exceed the local speed of sound. As the expansion continues the individual particles do not collide leading to a decreased collision rate. In this way temperature during the expansion can be decreases to a few K.

The temperature can be minimized by increasing the backing pressure or by decreasing the orifice diameter. In addition, the distance of the laser pulse from the orifice must be optimized. In the case of HHG from aligned molecules, a compromise between the high gas density (and thus high XUV signal) and the low temperature (which decrease as the gas density drops) needs to be made.

1.3.5 Detection of NAMA

NAMA was first proposed by Seidmann[48] and demonstrated experimentally from Rosca Pruna & Vrakking[49]. A typical experimental method for detecting the NAMA is through pump-probe experiments. The first pulse (pump) creates a rotational wavepacket and a second delayed pulse (probe) is monitoring the evolution of the angular distribution of the wavepacket as a function of time.

NAMA was first experimentally detected by inducing a Coulomb explosion on the molecular ensemble[50]. A linearly polarized pulse was used to align the molecules and a delayed second probe pulse to induce a Coulomb explosion of the molecules. The resultant atomic ion fragments were analyzed using time-of-flight mass spectrometer providing information for the angular distribution of the molecules.

The idea of detecting the molecular alignment using HHG came up almost simultaneously[8]. The experimental procedure again is similar. The probe pulse in this case is generating harmonics at variable delays. HHG from aligned molecules has been used among others for molecular orbital tomography[7,] elliptically/circularly polarized XUV radiation[51] and quantum interference effects[9,10].

NAMA has also been studied experimentally using transient birefringence[52,53], four wave mixing[54,55] and population measurement[56,57].

1.4 Elliptically/Circularly polarized XUV light from aligned molecules

HHG depends strongly on the polarization of the driving IR laser field. In HHG from atoms the three step model prohibits any HHG from circularly/elliptically polarized light. Thus, the XUV radiation in atoms is mainly generated by a linearly polarized driving field (figure 1.11- left panel). The reason is that an electron accelerated in an elliptically polarized field has lower probability to return to the parent ion since the transverse component of the electric field drives the wavepacket away (figure 1.11- middle panel). This results to a significant reduction of the emitted HHG radiation. The use of molecules (due to the larger size compared to atoms) as a generating medium increases the recollision probability and thus the harmonic yield (figure 1.11- right panel). We note that even in this case the harmonic yield remains, much lower compared to the yield generated by linearly polarized pulse. This effect has been used for the generation of circular polarized XUV radiation from aligned molecules as is described in chapter 4.

In order to further elaborate in this matter, firstly we will analyze the case of the generation of elliptically polarized XUV light using linear polarized IR pulse and later (in Section 4) we will describe how the used of elliptically polarized light can help towards the generation of near-circular polarized XUV light.

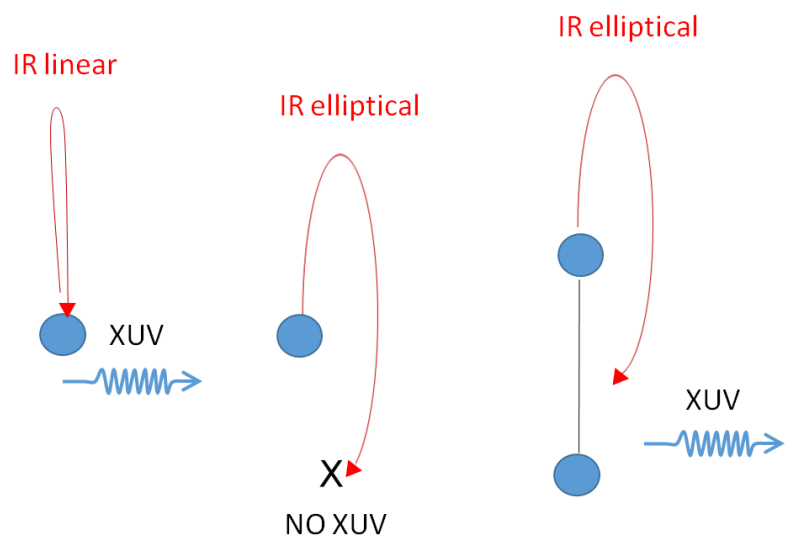

Figure 1.11: Illustration of HHG from an atom with a linear polarized IR field (left panel). HHG from atoms using an elliptical polarized IR field is restricted since the transverse component of the field drives away the electron from the atomic core (middle panel). The electron has a higher chance to return to the core in the case of molecules due the larger size compared to atoms. This way XUV radiation can be generated from an elliptically polarized driving field (right panel).

Elliptically polarized XUV radiation can be generated from a linear IR driving field using a sample of aligned molecules as a generation medium. If the polarizations of the pump and probe beams are parallel, the molecular angular distribution is cylindrically symmetric around the laser polarization. Thus, the induced dipole is parallel to the laser field direction and harmonic emission is always polarized along the laser polarization direction. By rotating the molecular axis with respect to the laser field the induced dipole can be decomposed to two orthogonal components, one parallel $d_{\parallel}$ and one perpendicular $d_{\perp}$ to the laser field direction (see figure 1.12). A component of harmonic emission perpendicular to the one parallel to the laser polarization can be generated[51]. Polarization properties depends not only on the amplitudes of the two perpendicular components of the harmonic field that must be equal but also on their phase difference $\delta = \Phi_{\parallel} - \Phi_{\perp}$. If the two components are of the same amplitude but their phase difference is 0 or π the XUV polarization is still linear but the nonzero perpendicular component rotates the harmonic polarization away from the laser polarization direction. For values of δ between 0 and π the polarization is elliptical and for the particular phase difference $\delta = \pi/2$ the harmonic polarization is circular. However, the ellipticity of the generated harmonics using a linear IR driving field does not exceed $\varepsilon \approx 0.35$[51]. The above conditions for the phase difference δ and the relative amplitudes of the two components can be achieved with the use

of near circularlly polarized driving IR field leading to harmonic emission with a high degree of ellipticity (close to circular) but lower yield as explained with details in chapter 4.

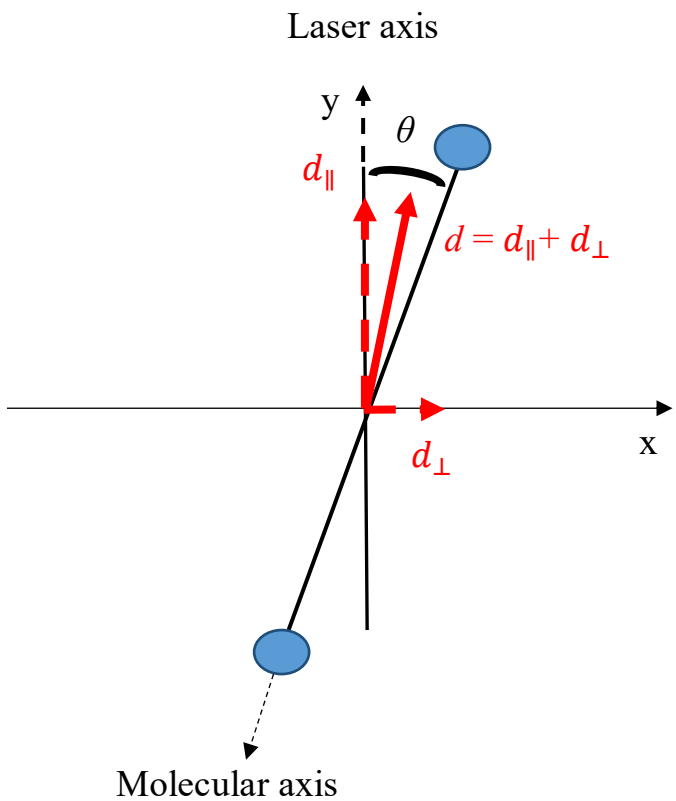

Figure 1.12: Schematic representation of the induced dipole moment d from a molecule aligned at an angle θ with respect to the laser field direction that contains a parallel $d_{\parallel}$ and a perpendicular $d_{\perp}$ component to the laser field direction.

Chapter 2

Imaging the source of high-harmonics using Time-gated Ion Microscopy

2.1 Introduction to Time-gated Ion Microscopy

The development of intense ultrashort radiation in the visible and extreme ultraviolet spectral range (VUV/XUV) has led to fascinating studies in the laser-matter interactions. In the majority of these studies the system under investigation interacts with a focused light beam which ionizes the system. The ionization products are usually measured by devices which spatiotemporally integrate the signal originating from the entire focal area. This way valuable information about ionization dynamics taking place in the interaction volume is discarded. With a recently developed approach based on an ion imaging device called 'Ion Microscope' (I-M), detailed information about the processes occurring at the source can be extracted. This approach is based on the record of images of the spatial distribution of ionization products produced in a focused beam from the Ion Microscope. Since ionization occurs at the focus of a radiating beam the ionization area is an image of the radiation source itself. This method will be described with more details in the next section.

For a long time two parameters intrinsic of the laser sources used in strong field ionization experiments have prevented the observation of several phenomena and/or the details of the effect under investigation. These are the temporal and spatial distributions of lasers' electric field amplitude. In contrast to linear processes, a challenge in the study of non-linear optics such as HHG is the study of phenomena at well confined space volumes and time intervals. The spatiotemporal laser field distributions in combination with averaging detection devices prevent (in many cases) the detailed study of laser matter-interaction.

The effect of temporal variation of the laser field amplitude is more pronounced for 'long pulses'[58]. The observation of the interaction products is averaged over many cycles and there is no way to limit it to a few cycles around the pulse peak intensity. The reason for that is that the atoms/molecules are fully ionized at the rising edge of the multi cycle laser field. The development of short pulses led to a reduction of the 'averaging' time and allowed the observation of non-linear optical interactions like HHG[4,30], above threshold ionization (ATI)[59-62] and direct double ionization[59,63-65].

Spatial integration of interaction products has been a further obstacle for the detailed study of strong field processes. 'Volume effects' due to the averaging of ionization products over the spatial intensity distribution in the focal volume has obscured the direct observation of ionization saturation and depletion of the atomic/molecular ground state, preventing straightforward quantitative measurements and reducing

the contrast of measurements[66,67]. Successful attempts for spatially resolved multi-photon ionization have been demonstrated already in the 1990s[68-71] . Recently, an advanced approach for spatially resolved measurements has been developed and implemented in the IR[72] and XUV[34,73] spectral range. It is based on the Ion Microscope which is a ion imaging device facilitating the observation of the spatial distribution of the ionization products produced in a focused beam as a function of their mass over charge ratio, m/q. Since the ionization process occurs in a focused radiation beam an immediate advantage in using this device is the observation of local intensity effects within the laser focus; saturation and aberration being two of those. It therefore facilitates quantitative measurements which are complicated when averaging volume signals are analyzed. A notable application of this device is the observation of intrinsic spatiotemporal properties of the radiation source. Thus, the ionization area is an image of the radiation source itself. The recorded images of the ion spatial distribution at the focus of the radiation reflect the spatial distribution of the radiation source, this being a HHG or a laser source.

2.1.1 Operation principle of the Ion Microscope

A schematic of the IM is shown in figure 2.1(a). The back reflected beam is focused into the interaction region with a spherical mirror. The interaction area is filled with the gas under investigation using a piezo pulsed nozzle. The ion distribution produced in the laser focus (located in the object plane) is mapped onto a position-sensitive detector located in the image plane. IM reveals the spatial distribution of charged particles in a magnified high-resolution manner in contrary to a velocity mapping spectrometer that images their momentum distribution. The ions generated at the focus of the laser beam are first accelerated by an electric field between the repeller (being floated at a voltage of V_{rep}) and extractor electrodes (being floated at a voltage of V_{ext}) placed at a distance ~ 0.7 cm from the repeller. A first electrostatic lens (EL1 placed at a distance ~ 2.5 cm from the repeller) images the spatial extent of the ion cloud on an intermediate ion image plane with a small magnification factor $M1$ ranging from 5 to 7. This intermediate image plane is located at a focal plane of a second electrostatic lens (EL2 placed at a distance ~ 15 cm from the repeller) that projects a further magnified image (the magnification factor of $M2$ is ranging from 20 to 30) onto the detector consisting of a pair of MCPs (placed at a distance ~ 50 cm from the repeller) and a phosphor screen. The image of the ion cloud that appears on the phosphor screen is magnified by a factor $M = M1 \times M2$ and is recorded in a CCD camera. The recorded images are the two dimension projections of the three dimension focal ion distribution. Since fragments with different mass to charge ratios have different flight times the detector can be gated with a few tens of ns time window for the imaging of the spatial distribution of a specific mass peak.

The spatial resolution of the IM depends on the DC applied voltages and the density of ions (space charge effects). This is due to the repulsive forces among the ions (space charge effects) from the generation

point until the detector. Optimization of the resolution can be achieved by reducing the density of ions and/or maximizing the operation voltages. The best experimentally reported spatial resolution is in the range of ~ 1 μm[34,73].

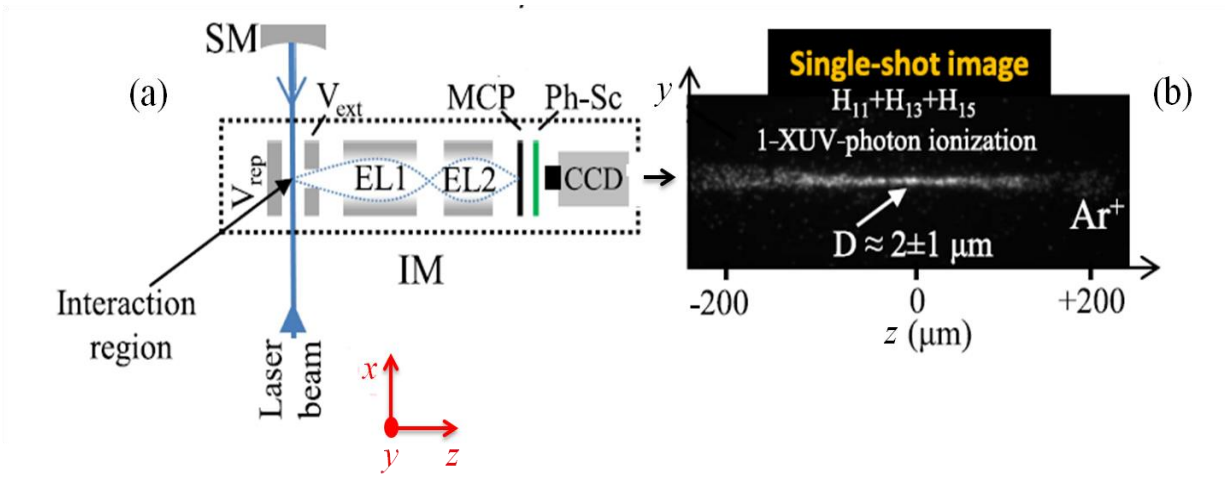

Figure 2.1: (a) Schematic representation of the operation principles of the I-M. The I-M consists of the interaction area where the laser pulse is focused and the electrostatic lenses EL1 and EL2 that are used for magnifying and imaging the ion distribution produced in the interaction region. (b) A typical single shot ion distribution at the focus of an XUV beam which contains harmonics from 11th to 15th. The ion distribution is produced through the 1-XUV photon ionization of Ar.

2.1.2 Applications of Ion Microscopy in the linear and non linear XUV spectral regime.

The measurement of the HHG intensity distribution at the focus of the XUV source is of great importance since it provides quantitative information about the properties of the source and the ionization dynamics of the system under investigation for both linear and non-linear ionization processes. For example the spatial ion distribution images have been used for quantitative studies of the 1-XUV ($\sigma^{(1)}$) and 2-XUV ($\sigma^{(2)}$)[73] ionizations cross sections and measurements of the order of non-linearity of the ionization process in the XUV region. The Ion Microscope has also been used for the measurement of the dynamics of the two interfering electron trajectories in the plateau region of the harmonic spectra[34]. These measurements will be described in the following section.

2.1.3 Mapping the HHG process

Kolliopoulos et al.[34] used the spatially resolved ion distribution images of 1-XUV photon ionization of Ar in order to measure the phase difference $\Delta\varphi^{L,S} = \varphi_q^L - \varphi_q^S$ between the 'Long' and 'Short' trajectories that contribute in the plateau region of the XUV radiation. From this measurement direct information of the difference (Δt_e) in the harmonic emission times and in electron quantum paths (ΔL_e) of the two trajectories can be obtained.

The two trajectories contribute to the Harmonic spectra with different induced phases $\varphi_q^{L,S} = \tau_q^{L,S} U_p$ that depend on the driving field intensity I_L (U_p is the ponteromotive energy that is proportional to the intensity I of the driving field and $\tau_q^{L,S}$ the flight times of the electron trajectories in the continuum) and different divergence[74]. Harmonics generated mainly from long electron trajectories depict an annular shape beam profile with larger divergence compared to harmonics generated mainly from the the short trajectories. The main idea behind the measurements was to focus together the two interfering spatial regions in a detector for different intensity values and record images of the focal area. The IM provide the necessary high spatial resolution for this project. Since the phase difference between the two trajectories are intensity dependent a single and double peak structure is expected to appear along the z-axis of the ion distribution for $\Delta\varphi^{L,S} = 2n\pi$ and $\Delta\varphi^{L,S} = (2n+1)\pi$ (where $n = 0,1,2,3..$) respectively.

Figure 2.2 (upper panel) shows this change of the ion distribution from a single to double peak structure with driving laser intensity I_L which is in fair agreement with the theoretical calculations (figure 2.2 down panel). The phase difference of the two trajectories can be deduced from the structure of the contour plot of figure 2.2 by using the three following considerations:

a) $\Delta\varphi^{L,S}$ = 0 for the low values of the driving field intensity I_L where an intensity independent single peak structure can be observed. This element is in agreement with the harmonic generation theory according to which, in the cut off region the two trajectories degenerate to one.

b) The $\Delta\varphi^{L,S}$ is increasing monotonically with I_L[75]

c) The $\Delta\varphi^{L,S}$ is increasing by π when the structure changes from a single peak to double and vice versa.

Taking into account the above considerations the values of $\Delta\varphi^{L,S} = n\pi$ (n=0 1,2,..) , $\Delta t_e = nT_q/2$ and ΔL_e can be obtained (more details in[34]).

(a)

(b)

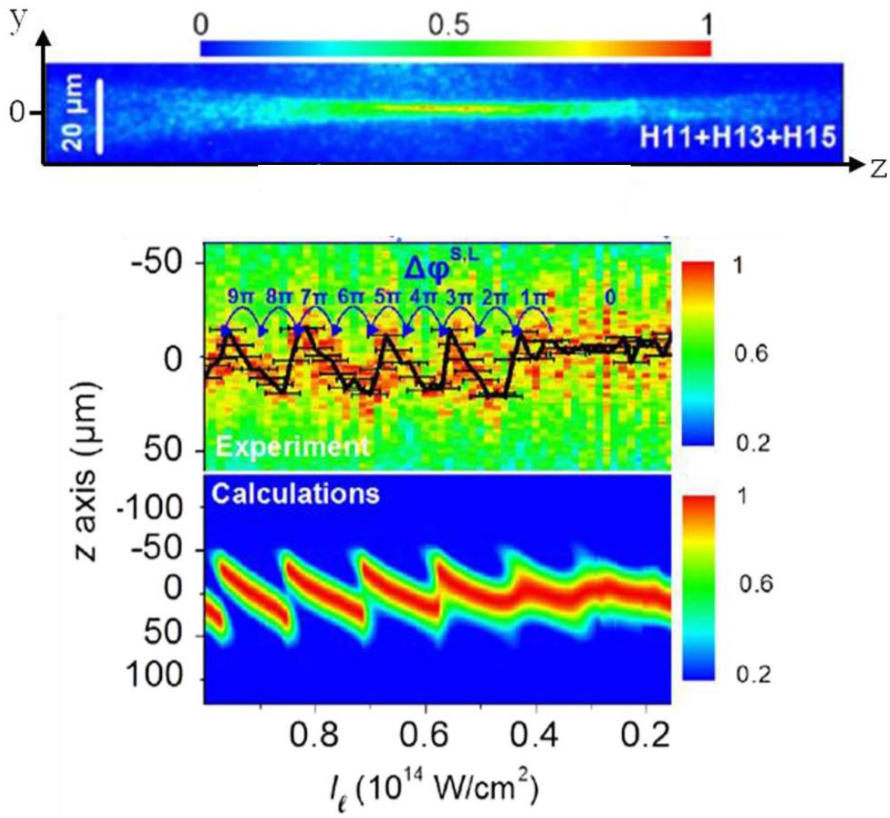

Figure 2.2: (a) Spatially resolved Ar^+ ion distribution produced by 1-XUV photon ionization process at the focus of the XUV beam. (b) The contour plot for the ion distribution of along the z-axis for different laser driven intensities I_L. Upper panel: the plot shows how the structure of the ion distribution along the z-axis of (a) changes from single- to double peak. The plot was produced after normalization of the line outs of the ion distribution along the z-axis at y=0. The black line depicts the mean value of the ion distribution. The error bars represent the standard deviation of the mean value resulting from the accuracy of the laser intensity measurement. Lower panel: calculation of the normalized contour plot.

2.2 Imaging the source of high harmonic using time gated Ion Microscopy

In atomic gases, it is well understood that in the strong field regime there are two electron trajectories within each laser half cycle, called the *long (L)* and the *short (S)*, with different excursion times in the continuum which contribute to emission at each harmonic frequency (see figure 1.1). It turns out that the different continuum excursion time manifest in different phase contributions to the *L* and *S* electron trajectories leading to distinctive interference features. Harmonic radiation which is generated mainly by the *L* trajectories present higher divergence than this generated mainly by the *S* one[74]. Furthermore, their

relative contribution to the outgoing from the medium harmonic beam can be controlled by the appropriate focusing geometry[76]. In spite of the knowledge acquired over the last two decades on the role of the electron trajectories on the spatial properties of the generated harmonic beam, in the majority of the experiments it is considered that the image of the XUV source is unaffected by the geometrical conditions in the HHG area. In particular, the influence of the relative position of the IR focus and the gas jet on the "virtual" position of the harmonic source has never been directly demonstrated experimentally.

The aim of the present study is to examine the dependence of the "virtual" position of the harmonic source on the laser focusing geometry using an Ion-Microscope (I-M) imaging detector. By "virtual" position here we mean the position at which the source has to be considered being placed in order to produce the measured image after refocusing of the XUV beam. I-M allows the recording of the spatial distribution of the ionization products produced by a (usually focused) beam and consequently the spatial intensity distribution of the ionizing XUV radiation. Taking advantage of the high spatial resolution of the I-M we have been able to study the variation of the XUV focus position as a function of the relative position of the gas medium and the IR focus. This is realized by varying the position of the gas medium and recording the spatial ion distribution of Ar produced by a single-XUV-photon ionization process at the focus of the XUV beam keeping the position of the IR focus constant.

2.2.1 Experimental Results

The experiment is performed utilizing a 10 Hz Ti:Sapphire laser system delivering 25 fs long laser pulses with central wavelength 800 nm and energy ≈15 mJ/pulse. The experimental set up is shown in Fig. 2.3(a). The laser beam is focused with a f = 3m lens (L) into a pulsed gas jet (P-GJ) with a rectangular orifice with dimensions 0.3 mm x 1 mm, filled with Ar gas. The gas jet is mounted on a translation stage allowing the variation of the position of the jet with respect to the IR focus. The IR radiation is eliminated after the XUV generation by a combination of a reflection on a silicon plate (Si) placed at the Brewster angle of the IR beam, a 5-mm diameter aperture (A) and a 150 nm thick Sn filter which transmits the harmonics (q) from 11th to 15th. Subsequently, the XUV radiation is focused into the target gas jet (T-GJ) filled with Ar by a spherical gold mirror (SM) of 5 cm focal length. Care has been taken to fix the angle of incidence of the XUV beam on the gold mirror at ≈ 0°. The SM is placed 4.5 m downstream the P-GJ. The images are monitored by the transversely placed I-M which records the spatial distribution of Ar ions as described above (Fig. 2.3(b)).

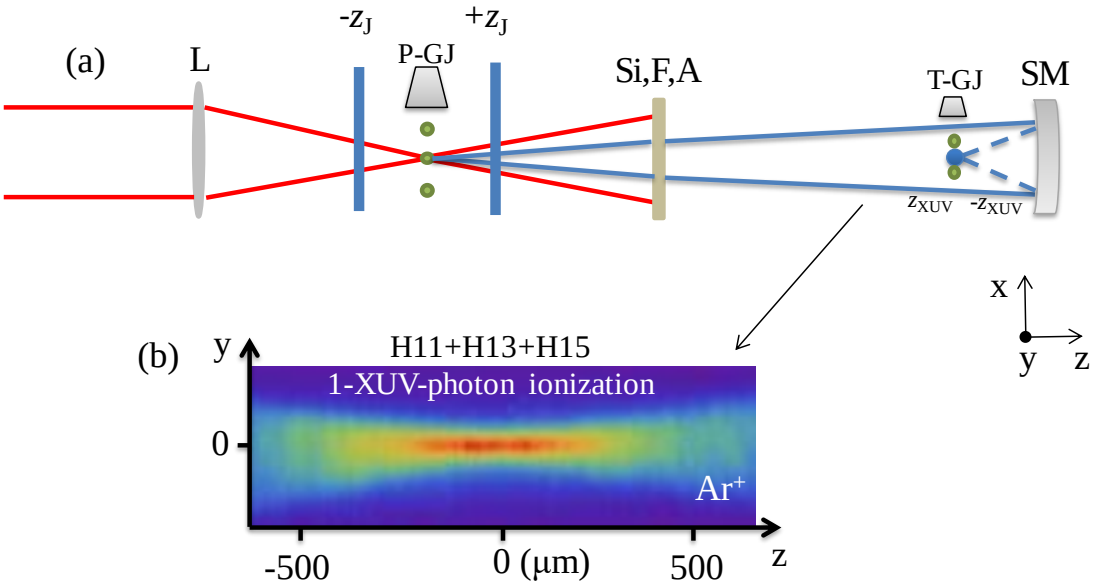

Figure 2.3: (a) Schematic of the experimental set-up. L: Lens P-GJ: Pulsed gas jet used for the HHG mounted on translation stage of micrometer precision; Si: Silicon plate, A: Aperture, F: Filter, T-GJ: Target gas jet, SM: Spherical mirror (b) A typical image of Ar^+ spatial ion distribution produced by a single-XUV-photon ionization process at the focus of the XUV beam, as it was retrieved by the I-M (with a magnification $M \approx 50$) after the accumulation of 600 shots. The XUV beam in the T-GJ area consists the harmonics from 11th to 15th with relative amplitudes 0.6(11th):1(13th):0.8(15th).

We vary the position (z_j) of the pulse gas jet P-GJ from $z_j \approx -3$ cm to $z_j \approx +3$ cm with a step of 3 mm while recording the XUV focus distribution (in y-z plane in Fig. 2a) and location (along z) with respect to the P-GJ position corresponding to each z_j. The range of the scan of the P-GJ is almost coinciding with the full confocal parameter b ≈ 7 cm of the focused driver. In the single XUV photon ionization limit, the HHG yield is proportional to the total ion yield measured by I-M. By spatially integrating the recorded images we have obtained the dependence of HHG yield on the position of the P-GJ (Fig. 2.4 (a)).

The dependence of the XUV focus position (z_{XUV}) on the position of P-GJ is shown in Fig. 2b. The position of the XUV focus was defined by the maximum of the ion distribution obtained from the lineout at y=0 along the propagation axis (z) (Fig. 2.4.(b)). The maximum was obtained by the zero of the derivative of the line outs. In order to avoid the noise introduced in the derivative by the fine structure (of few pixel size) of the ion distribution, the line outs have been smoothed over 70 points. The overall displacement of the z_{XUV} found to be ≈ 20 μm and cannot be explained by the 6 cm movement of P-GJ (which can provide

a maximum displacement of ≈ 7.6 μm at the XUV focus). Considering that i) for a specific position of the P-GJ, ii) the non-linearity of the HHG process results to a HHG yield $\propto (I_L)^p$ where I_L is the intensity of the laser and p = 3-5 for all plateau harmonics[77] and assuming that all the harmonics are emitted from the same cross section in the gas medium, , the observed displacement is attributed to the different wave front curvature, which for Gaussian beams essentially means to the different divergence of the XUV beams resulting from the L and S trajectories. Particularly it was shown[78] that the dependence of the divergence on the electron trajectories for the harmonic order q is given by $\theta_{S,L} = \frac{\lambda_q}{\pi w_q}\sqrt{1 + 4\alpha_{S,L}^2 I_L^2 \frac{w_q^4}{w_f^4}}$ (eq.1) (where λ_q, w_q, are the wavelength and the beam waist of the harmonic q, w_f is the waist size of the laser beam and $\alpha_{S,L}$ is the S, L trajectory coefficient), which results in $\theta_S/\theta_L = \sqrt{(1 + A\alpha_S^2)/(1 + A\alpha_L^2)} \approx \alpha_S/\alpha_L$ (eq.2). Although the contribution of both electron trajectories at each P-GJ position cannot be excluded[79] , in the present study we can safely consider that for $z_j \approx +3$ cm ($z_j \approx b/2$, where b is the confocal parameter and b ≈ 7 cm) and $z_j \approx -3$ cm the main contribution is coming from the S and L trajectory harmonics, respectively. Differences that phase matching imposes to the radiation emitted by the two different quantum trajectories such as the different divergence of them, have already been established before. They have been studied in the past[74,76] and verified in the present work by measuring the width of the line out along the propagation axis for each position of the P-GJ (Fig.2.4 (c)). It is evident that for $z_j \approx 0$ where both trajectories have significant contribution to the harmonic emission[34], the width of the distribution along the propagation axis is ≈ 1.5 times larger than the width measured at $z_j \approx \pm 3$cm where the main contribution is coming from single trajectory harmonic.

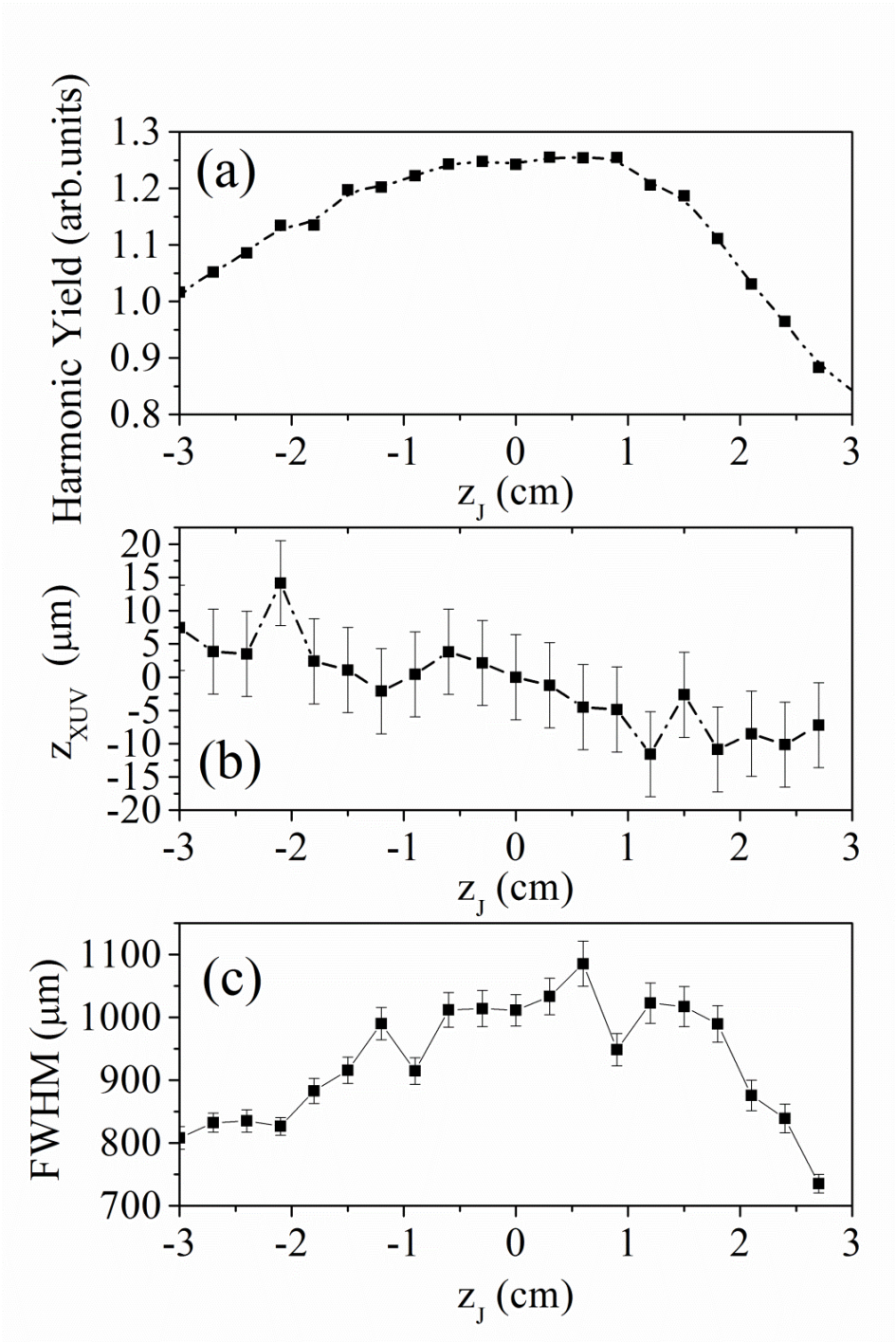

Figure 2.4: (a) Spatially integrated Ar^+ ion signal produced by a single-XUV-photon ionization process at the focus of the XUV beam as a function of the gas jet position (b) XUV focus position as a function of the gas jet position. The error bars represent one standard deviation of the mean value. (c) FWHM of the XUV focal distributions resulting from a gaussian fit as a function of the gas jet position. The error bars correspond to the error of the FWHM after the gaussian fit of the lineouts. 600 shots were accumulated for each image.

Thus, considering as central wavelength of the XUV the 13th harmonic (λ_h= 61.5 nm), $\alpha_S \approx 2.5\text{x}10^{-14}$ rad cm^2/W, $\alpha_L \approx 22.5\text{x}10^{-14}$ rad cm^2/W [80], and $w_f = w_q \approx 150\mu m$[78], the above relation results to $\theta_S/\theta_L \approx 0.12$. Utilizing geometrical optics, this ratio leads to a distance of $\Delta z_{obj} \approx 22$ cm between the "virtual" positions of the *S*, *L* trajectory-harmonics sources and results to an overall displacement of $\Delta z_{XUV} \approx 23$ μm at the focus of the XUV. Incorporating the displacement introduced in P-GJ this value is in excellent agreement with the experimental findings. Figure 2.5 shows a schematic which depicts the "virtual" positions of the harmonic source (V_S and V_L) and the corresponding XUV foci at z_j = -3 and z_j = 3 (Im_L and Im_S, respectively).

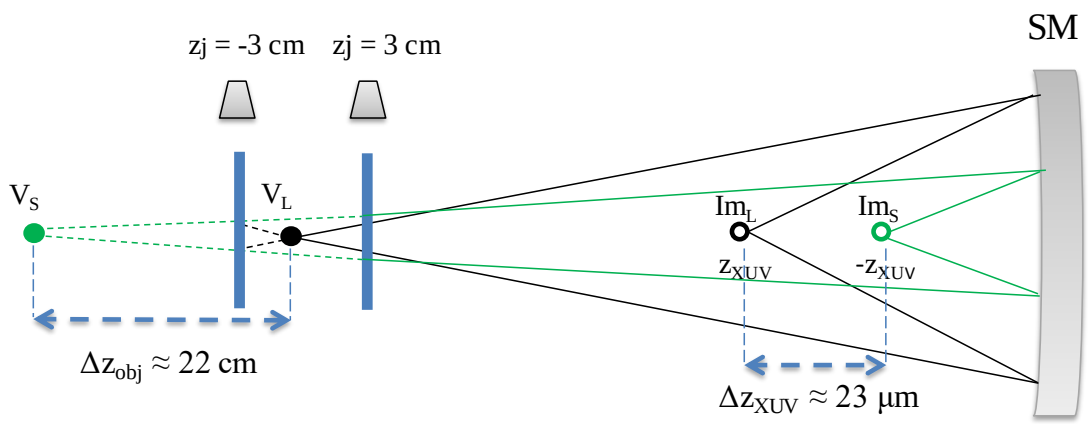

Figure 2.5: By varying the generation jet position from $z_j \approx$ -3 cm to $z_j \approx$ 3 cm "virtual" positions of the harmonic source are resulted due to the varying divergence difference of the harmonic radiation emitted by the *S* and *L* trajectories (blue vertical line). At the jet position z_j = -3 cm the *L* trajectories with higher divergence (black dashed lines) dominate the harmonic emission leading to a "virtual" positions of the harmonic source V_L. On the contrary, at the jet position z_j = 3 cm the *S* trajectories with smaller divergence (green dashed lines) dominate the emitted radiation leading to a "virtual" positions of the harmonic source V_S. The difference of the position of the "virtual" sources is $\Delta z_{obj} \approx 22$ cm. This difference in the "virtual" positions should lead to a $\Delta z_{XUV} \approx 23$ μm displacement of the XUV focus position (Im_L and Im_S) after the reflection on the spherical mirror which is in accordance with the geometrical optics and in fairly good agreement with the measured experimental value of ≈ 20 μm.

Generally, the divergence changes with harmonic order. In this work we measure the average effect of all three not resolved harmonics involved (11, 13, 15) and the calculations are done for the central one i.e. the 13th harmonic. This is justifiable because applying (eq. 1) to all three harmonics one can easily extract that the ratio θ_L/θ_S is essentially the same for all three harmonics, namely, 0.112, 0.113 and 0.111

for the 11th, 13th and 15th harmonic respectively. While the atomic dipole phase is an unambiguous factor contributing to the effect at hand other propagation effects such as defocusing due to ionization and/or third order non-linearities[81,82] are much less probable, as I) the intensity was safely kept below saturation, II) the medium we use is very short compared to the confocal parameter and III) such phenomena is expected to have the same effect on both trajectories. Nevertheless, our experimental approach can be used also for the study of such phenomena whenever they become relevant.

2.4 Conclusion

In conclusion, by utilizing a time gated ion microscopy technique, we demonstrate that the image of the XUV source is affected by the geometrical conditions in the HHG area. Particularly, it was found that the short- and long-trajectory harmonics generated in gas phase media are focused in different positions in the detection area. This was measured by recording the of spatial ion distribution produced by single-XUV-photon ionization process at the XUV focus for different relative positions of the IR focus and the gas jet. Access to such online source positioning allows better control and provides increased possibilities in experiments where selection of electron trajectory is important. The present study gives also access to quantitative information which is connected to the divergence, the coherence properties and the photon flux of the harmonics. Finally, it constitutes a precise direct method for providing complementary experimental info to different attosecond metrology techniques.

Chapter 3

Quantum path interferences in high–harmonic generation from aligned diatomic molecules

3.1 Introduction

In this work, by employing a self–reference approach, we demonstrate the existence of the quantum path interference effects in strong–laser–field molecular physics and we measure their dependence on the molecular orientation. Specifically, we show that the presence of (S) and (L) quantum paths in the harmonic generation is of significant importance for accessing intricacies associated with the dependence of the dynamics of recollision process on the molecular structure. By exploiting the beneficial experimental simplification of using only a single-XUV beam produced by the S– and L–electron trajectories of aligned N_2 molecules, we reveal that the spatial intensity distribution around the XUV focus carries the information of the harmonic generation process during the molecular alignment. This is achieved by combining the time gated ion spectroscopy with a pump-probe arrangement. The pump – probe arrangement is used to trigger the alignment process (IR pump pulse) and generate the high-harmonics (IR probe pulse). The alignment dynamics can be obtained by measuring the dependence of the spatially integrated harmonic yield on the delay between the pump and the probe pulses, while the spatially resolved intensity distribution around the focus is used to measure the dependence of the quantum path interference, resulting from the superposition of the S and L trajectory harmonics, on the molecular orientation. In the last part of this chapter the influence of the plasma generation on the spatial characteristics of the emitted XUV radiation is studied by resolving the intensity distribution around the focus for two different pump pulse intensity values.

3.2 Experimental set up

The experiment is performed utilizing a 10 Hz Ti:Sapphire laser system delivering ≈ 25 fs linearly polarized laser pulses with central wavelength at ≈ 800 nm and energy ≈ 40 mJ/pulse. The experimental setup is shown in Fig. 3.1. The laser beam was divided in two providing a sequence of pulses with adjustable delay. The pump pulse was used to trigger the process of the molecular alignment. In order to improve the degree of alignment, the pump pulse has been temporally stretched to ≈ 100 fs by inserting two BK7 plates of ≈ 2 cm total thickness in the pump path. The probe pulse was fully compressed and used to generate the high-harmonics. Both pulses were focused by a 3-m focal length lens and crossed at a small angle (≈ 2 deg) into a pulsed jet filled with N_2 gas. The two foci were placed close the N_2 jet favoring the harmonic emission from the short (S) and long (L) electron trajectories[83,74,79]. The intensity of the pump and probe beam was

independently controlled by means of apertures placed at each branch of the pump–probe set–up. The intensity of the pump in the interaction region was adjusted in order to have the optimum molecular alignment conditions ($I_L^{(pump)}$ ≈5×10^{13} W/cm^2) and for the probe pulse was set just below the saturation intensity of the harmonic generation process ($I_L^{(probe)}$ ≈10^{14} W/cm^2). After the N_2 jet, a Si plate was placed at Brewster's angle for the fundamental (75°) to reflect the harmonics towards the detection area, where the IM was placed, while substantially attenuating the IR probe beam. The XUV radiation, after reflection from the Si plate, passes through a 5-mm-diam aperture (A) and a 150 nm thick Sn filter which transmits the harmonics (q) from 11th to 15th (with relative amplitudes 0.6 (11th):1(13th):0.8(15th)) and blocks any residual part of the IR probe beam. Subsequently, the XUV beam was focused into the Argon gas jet by a spherical gold mirror (SM) of 5 cm focal length. Care was taken to fix the angle of incidence of the XUV beam on the gold mirror at 0 deg. The images were monitored by the transversely placed IM (having a magnification of $M \approx 100$ which records in an area of $200\ \mu m\ \times 60\ \mu m$ the spatial distribution of Ar ions produced at the focus of the XUV beam (left panel of Fig. 3.1b). The beam profile at a distance ≈ 140 μm away from the focus shows the contribution of the S– and L–trajectory harmonics (right panel of fig.3.1b). Because the distribution is produced by single-XUV-photon ionization process, the images correspond to the intensity distribution of the XUV radiation. We note that the harmonics used in the experiment are lying in the low photon energy region of the plateau harmonic spectrum and thus it is considered that are generated mainly by the HOMO molecular orbital[84]. Additionally, the contribution of the two–center interference effect1,[9] was neglected as the electron wavelength ($\lambda_e \approx 0.27\ nm$) corresponding to the emission of the 11th–15th harmonics is larger than the $R \approx 0.1\ nm$ internuclear distance of the N_2 molecule.

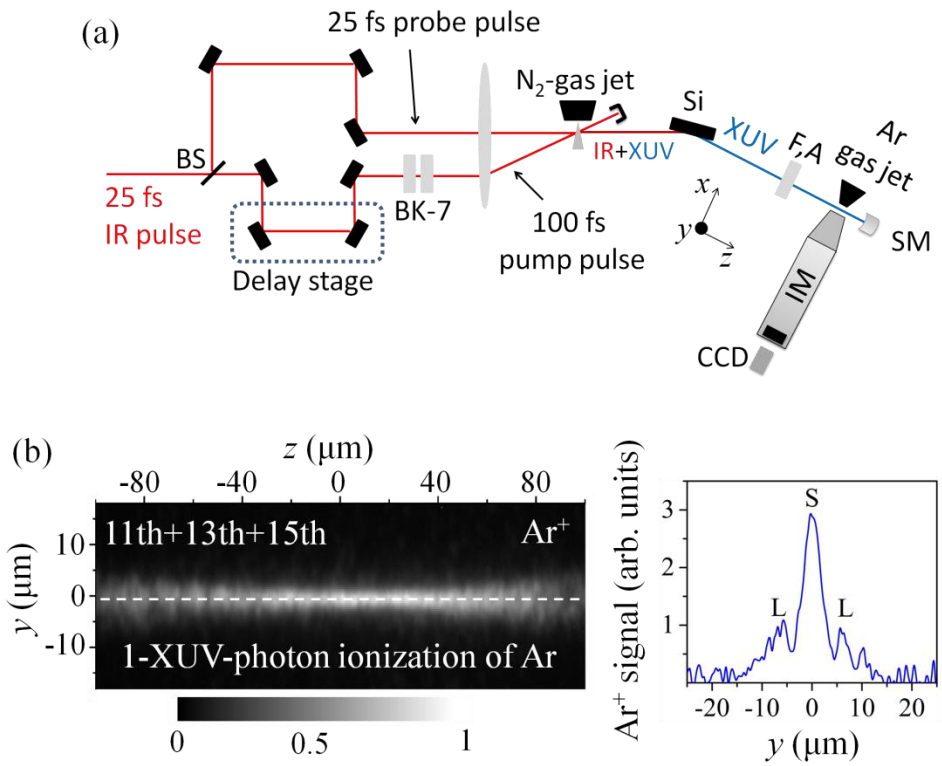

Figure 3.1: (a) Experimental set up. BS: Beam splitter, M: Mirrors, L: Focusing Lens, P-GJ: Pulsed gas jet, Si: Silicon plate, F: Filter, A: Aperture, T-GJ: Target Gas Jet, SM: Spherical mirror. (b) (left panel) Ar+ distribution induced by single–XUV–photon ionization process around the focus of the XUV beam consisting the harmonic 11th, 13th and 15th. 600 shots were accumulated for each image. (right panel) XUV beam profile ≈ 140μm away from the focus showing the contribution of the S–and L–trajectory harmonics.

3.3 Results

The evolution of the molecular alignment was traced by integrating the spatial Ar^+ distribution at $x = 0$, $y = 0$, z (white dashed line in the left panel of Fig. 3.1b) for each delay (τ) between the pump and the probe pulses. In particular, the recorded trace shows the dependence of the XUV yield on the molecular orientation during the evolution of the field–free alignment process. In agreement with the findings of ref.[1,7,46] the harmonic yield depicts a modulation every $\tau \approx Tr/4$ (where $Tr \approx 8.4$ ps is the rotational period of N_2) i.e. at $\tau \approx 2.1$ ps, $\tau \approx 4.2$ ps, $\tau \approx 6.3$ ps and $\tau \approx 8.4$ ps (Fig. 3.2). The maximum (at $\tau \approx 4.1$ ps and $\tau \approx 8.5$ ps) and minimum (at $\tau \approx 4.3$ ps and $\tau \approx 8.3$ps) values correspond to the times that the molecular axis is parallel and perpendicular to the polarization of the probe beam, respectively.

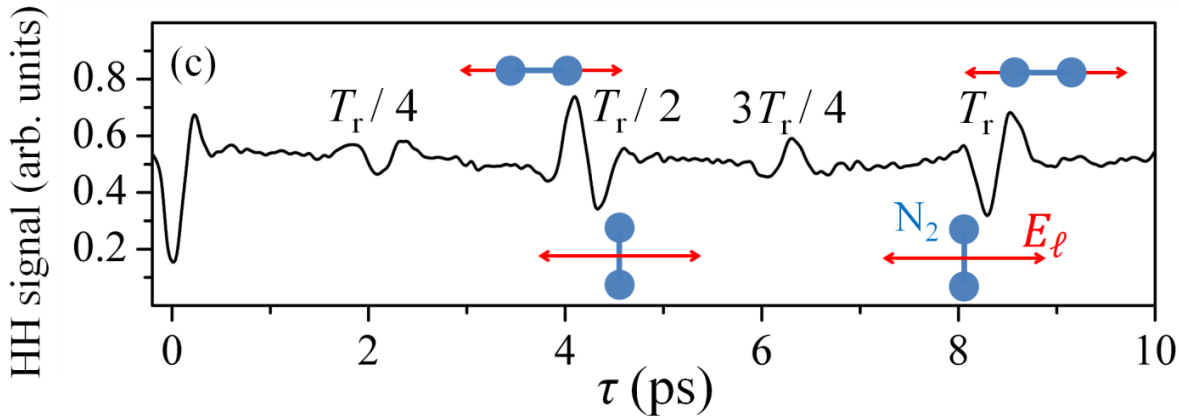

Figure 3.2: Harmonic signal as a function of the delay τ between the pump and the probe pulses. T_r is the rotation period of N_2. The panel shows the orientation of N_2 axis with respect to the polarization of the probe laser pulse around T_r and $T_r/2$.

The dependence of the dynamics of the S- and L– electron quantum paths on the orientation of the molecular axis is reflected in the spatial XUV intensity distribution along the propagation z –axis around the XUV focus. Figure 3.3 shows the line outs of the Ar^+ distribution at $x = 0$, $y = 0$, z as a function of τ. Besides the periodic modulation of the amplitude (shown in Fig. 1c), the width w of the line outs (measured at the full–width of half maximum of the recorded signal) also depicts a clear modulation every $\tau \approx Tr/4$ (pink–dashed–dot line in Fig. 3.3). The latter is attributed to interference effects exhibited in the XUV intensity distribution pattern due to the spatiotemporal overlapping of the harmonics emitted by S and L interfering electron quantum paths[34]. When the S– and L–electron trajectories contribute to the harmonic emission, the width of the intensity distribution along the XUV focus depends on the phase difference $\delta\varphi_q^{S,L} = \varphi_q^S - \varphi_q^L$ (where $\varphi_q^{S,L}$is the phase of the qth harmonic emitted by the S- and L- electron trajectory respectively) of the S- and L- trajectory harmonics. For $\delta\varphi_q^{S,L} = 2n\pi$ $(n = 0,1,2)$ the interference results in an intensity distribution having a single peak structure (narrow width) while for $\delta\varphi_q^{S,L} = (2n+1)\pi$ the distribution is broader having double peak structure.

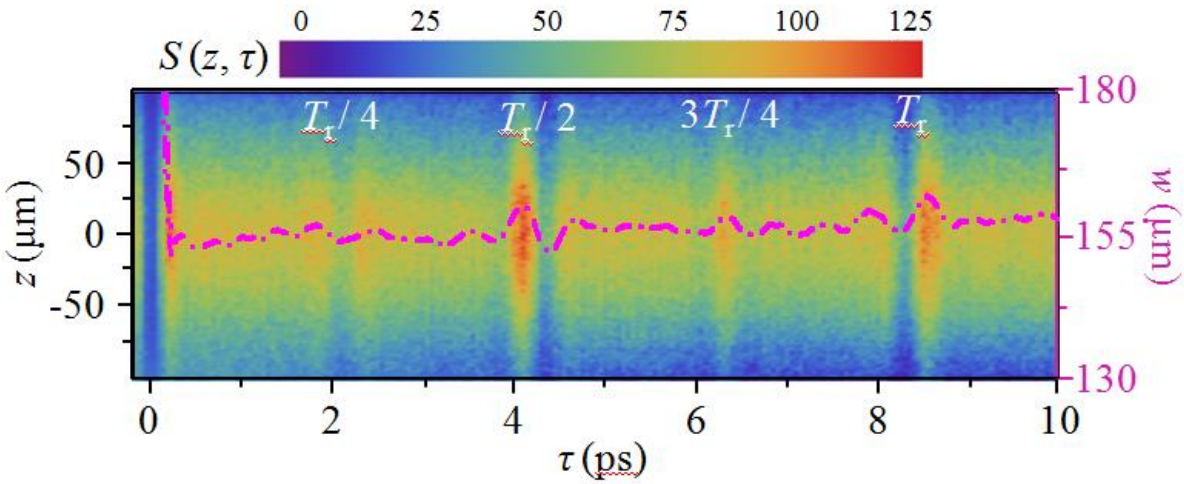

Figure 3.3: Line outs of the Ar^+ distribution at $x = 0$, $y = 0$, z as a function of τ. The pink dashed line shows the width w of the line outs as a function of τ.

In HHG from atoms, $\delta\varphi_q^{S,L} \approx U_p \delta\tau_q^{S,L} \approx -(\delta\alpha_q^{S,L}) I_l$ where U_p and I_l is the ponderomotive energy and the intensity of the driving laser field respectively. $\tau_q^{S,L}$ are the travelling times of the S and L trajectory leading to the emission of the qth harmonic and for Ar atom $\delta\alpha_q^{S,L} \approx 20 \times 10^{-14}\ rad \cdot cm^2/W$[31] is a constant (which depends on the ionization potential IP of the atom) corresponding to the difference of the phase coefficient $\alpha_q^{S,L}$ of the qth harmonic. In this case, the phase difference $\delta\varphi_q^{S,L}$ can be measured by varying the I_l.

In an anisotropic system such as a linear molecule, $\delta\varphi_q^{S,L}$ also depends on the relative orientation of the molecular axis and polarization of the driving field[8]. In the present work, because I_l is constant the change of the width w is attributed to the dependence of the $\alpha_q^{S,L}$ on the angle θ between the molecular axis and the polarization of the driving field, i.e $\delta\varphi_q^{S,L}(\theta) \approx U_p \delta\tau_q^{S,L}(\theta) \approx -(\delta\alpha_q^{S,L}(\theta)) I_l$. Due to the dependence of the tunneling rate on the coupling $d \cdot E_l$ (where d is the induced transition dipole moment and E_l is the laser electric field) it is shown that the ionization rate[46,84-86] and the efficiency of the HHG process[7,87,88] drops by a factor of ~ 6 when the orientation of the N_2 axis changes from parallel to perpendicular with respect to the polarization of the driving field. To calculate $\delta\varphi_q^{S,L}(\theta)$ and $\delta\alpha_q^{S,L}(\theta)$ we have used the ionization rates calculated by Ann-Thu Le et al.[84] and Z.X. Zhao et al[85] employed with molecular tunneling ionization theory[37] (MO-ADK). Then we have solved the semi-classical three-step model[6] for Ar atom in an intensity range (from $I_l^{max} \approx 10^{14}\ W/cm^2$ to $I_l^{min} \approx 8 \times 10^{13}\ W/cm^2$) which provides ionization rates that are matching those given by the MO-ADK theory i.e $W(I_l^{max})/\ W(I_l^{min}) \approx$

6. We note that Ar was selected as it is very similar to N_2 in its response to the strong laser field having almost the same IP (IP_{Ar} = 15.76 eV and IP_{N_2}= 15.58 eV) and intensity dependent ionization probability[89]. Figure 3.4a shows the calculated $\delta\varphi_q^{S,L}(\theta)$ and figure 3.4b the corresponding $\delta\alpha_q^{S,L}(\theta)$for q=11,13,15. We note that Ar is used only to facilitate the theoretical calculations and does not play the role of an auxiliary experimental reference. From figure 3.4a, it is evident that when the molecular axis changes from θ = 0 to θ = 90 degrees with respect to the laser polarization, the value of $\delta\varphi_q^{S,L}$ depicts an average shift of $\Delta \approx 1.4\,\pi$. $\Delta = \delta\varphi_{\parallel}^{S_{\parallel}L_{\parallel}}$- $\delta\varphi_{\perp}^{S_{\perp}L_{\perp}}$,$\delta\varphi_{\parallel}^{S_{\parallel}L_{\parallel}} = \langle\delta\varphi_{\parallel}^{S_{\parallel}L_{\parallel}}(\theta = 0)\rangle$, $\delta\varphi_{\perp}^{S_{\perp}L_{\perp}} = \langle\delta\varphi_{\perp}^{S_{\perp}L_{\perp}}(\theta = 90)\rangle$ and $\langle\delta\varphi^{S,L}(\theta)\rangle = \left[\sum_{q=11}^{15} A_q\delta\varphi^{S,L}(\theta)\right]/\sum_{q=11}^{15} A_q$, where A_q is the harmonic amplitude and $S_{\parallel},L_{\parallel}$, $S_{\perp}L_{\perp}$ are the electron trajectories for θ = 0 degrees (∥) and θ = 90 degrees (⊥) respectively.

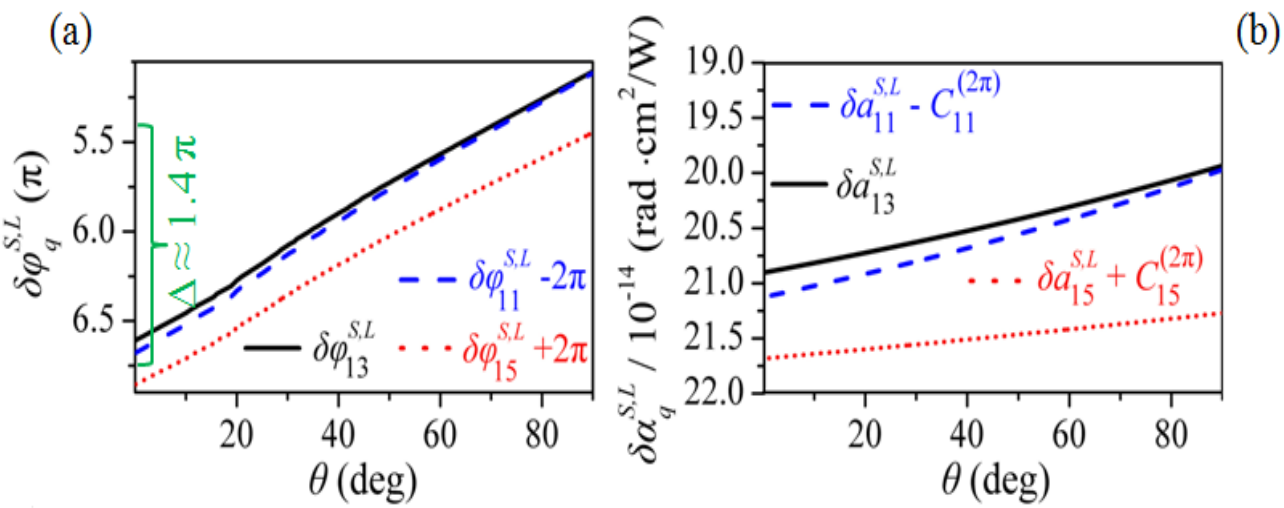

Figure 3.4: (a)The calculated $\delta\varphi_q^{S,L}(\theta)$ and (b) the corresponding $\delta\alpha_q^{S,L}(\theta)$ for q=11,13,15. $C_{11,15}^{2\pi}$ correspond to the values of $\delta\alpha_{11,15}^{S,L}$ calculated for a constant $\delta\varphi_{11,15}^{S,L}$= 2π,

The electron trajectories for the two extreme cases are illustrated in figure 3.5. Since the detected signal results from a harmonic superposition, hereafter, the term $\delta\varphi_q^{S,L}$ is replaced by $\langle\delta\varphi^{S,L}\rangle$. The fact that the value of Δ exceeds the value of π supports the presence of quantum path interference effects which are expected to be more pronounced around the revival times where the width w depicts a strong modulation.

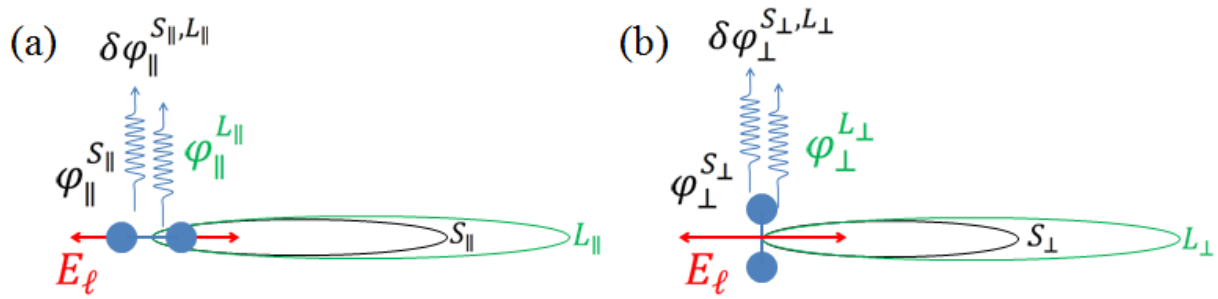

Figure 3.5: A schematic of the dependence of $\delta\varphi^{S,L}$ on θ for the extreme cases of(a) $\theta = 0$ and (b) $\theta =$ 90 degrees.

To make the interference effects clearer in the measured data (shown in figure 3.3) and ensure that the modulation of the width w is not influenced by the modulation of the harmonic yield $Y(\tau)$, from each line out of the raw data we have subtracted a normalized to $Y(\tau)$ backround signal $S_{BKG}(z, \tau_{rand})$ obtained by averaging the line outs in the region of $0.5\text{ps} < \tau_{rand} < 1\text{ps}$ where the molecules are nearly randomly oriented, i.e $S'(z,\tau) = S'(z,\tau) - S_{BKG}(z,\tau_{rand}) \cdot Y(\tau)/\langle Y(\tau_{rand})\rangle$, where $\langle Y(\tau_{rand})\rangle$ is the average harmonic yield in the region of τ_{rand}. For reasons of simplicity, the coordinates $x = 0$ and $y = 0$ are omitted from the equation. The resulted signal $S'(z,\tau)$ is shown in figure 3.6. A clear single and double peak structure with respect to $z \approx 0$, corresponding to a phase difference of $\langle\delta\varphi^{S,L}\rangle \approx 2n\pi$ and $\langle\delta\varphi^{S,L}\rangle \approx (2n+1)\pi$, respectively, appeared in the regions of $\tau \approx Tr/2$ and $\tau \approx Tr$. In the regions where the molecules are randomly oriented no pronounced structure was observed.

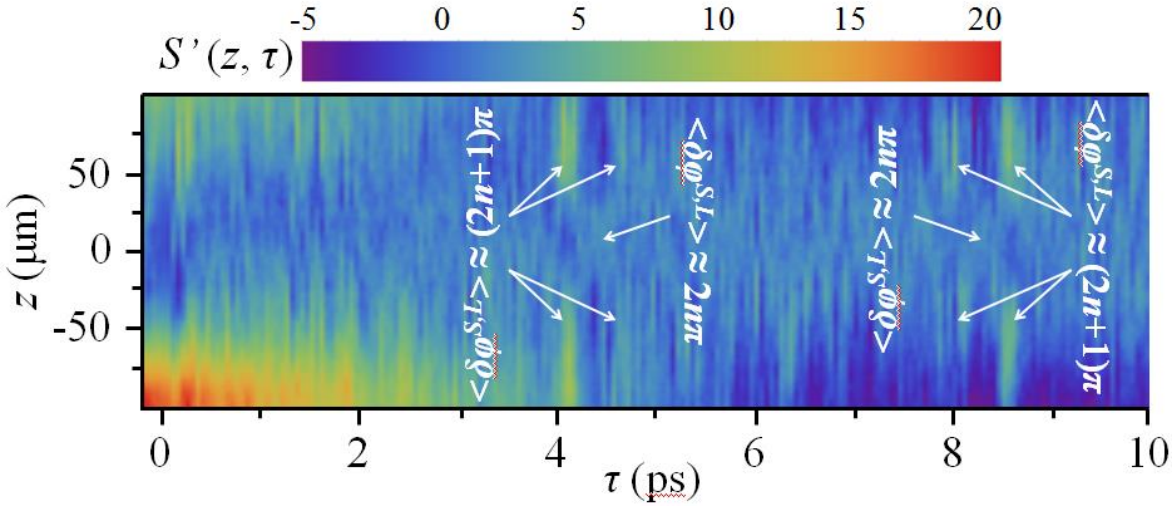

Figure 3.6 Line outs of the Ar+ distribution at x = 0, y = 0, z as a function of τ after the background subtraction process. The white arrows depict the distinct areas around *Tr* and *Tr/2* where the double and single peak structure along the z–axis is evident.

For the $I_L^{(probe)}$ used in the present experiment, the double and single peak structure appeared at $\tau \approx$ 4.06 ± 0.05 ps and $\tau \approx$ 4.35 ± 0.05 ps, respectively (Fig. 3.7a). These values are very close to $\tau \approx 4.1$ ps and 4.3 ps for which the squeezing of the angular distribution of the molecules around θ = 0 and 90 degrees, respectively, is maximum, as shown by comparing figures 3.2, 3.3 and 3.6. These have been also confirmed by the analysis of the interference pattern in the region around $\tau \approx Tr$. The results are in fair agreement with theoretical calculations shown in figure 3.7b and 3.8. Figure 3.7b shows the calculated dependence of the intensity distribution (normalize to unity) along the z-axis of the focus as a function of θ. The distribution was obtained by calculating the images of the focused harmonic beam with the phases $\langle\delta\varphi^{S,L}\rangle$ used to obtain figure 3.4. The measured relative harmonic amplitudes and the measured S- and L–trajectory harmonic beam profile shown in the right panel of figure 3.1b. We note that (besides a marginal constant Gouy phase shift which is included in the calculations of Fig. 3.7b) the spatiotemporal coupling effects[90,91] in the harmonic generation area have negligible dependence on θ and thus have been neglected from the analysis. Figure 3.7c shows the comparison between the measured (red-crossed triangles) and the calculated (black line) values of $\langle\delta\varphi^{S,L}\rangle$. The images are calculated by the Debye integral[92] after applying the Huygens-Fresnel principle on a spherical mirror with a 10 cm radius of curvature as shown in figure 3.8a. Figures 3.8b and 3.8c shows the calculated images of the interference pattern around the focus for $\langle\delta\varphi^{S,L}\rangle \approx 2n\pi$ and $\langle\delta\varphi^{S,L}\rangle \approx (2n+1)\pi$, respectively.

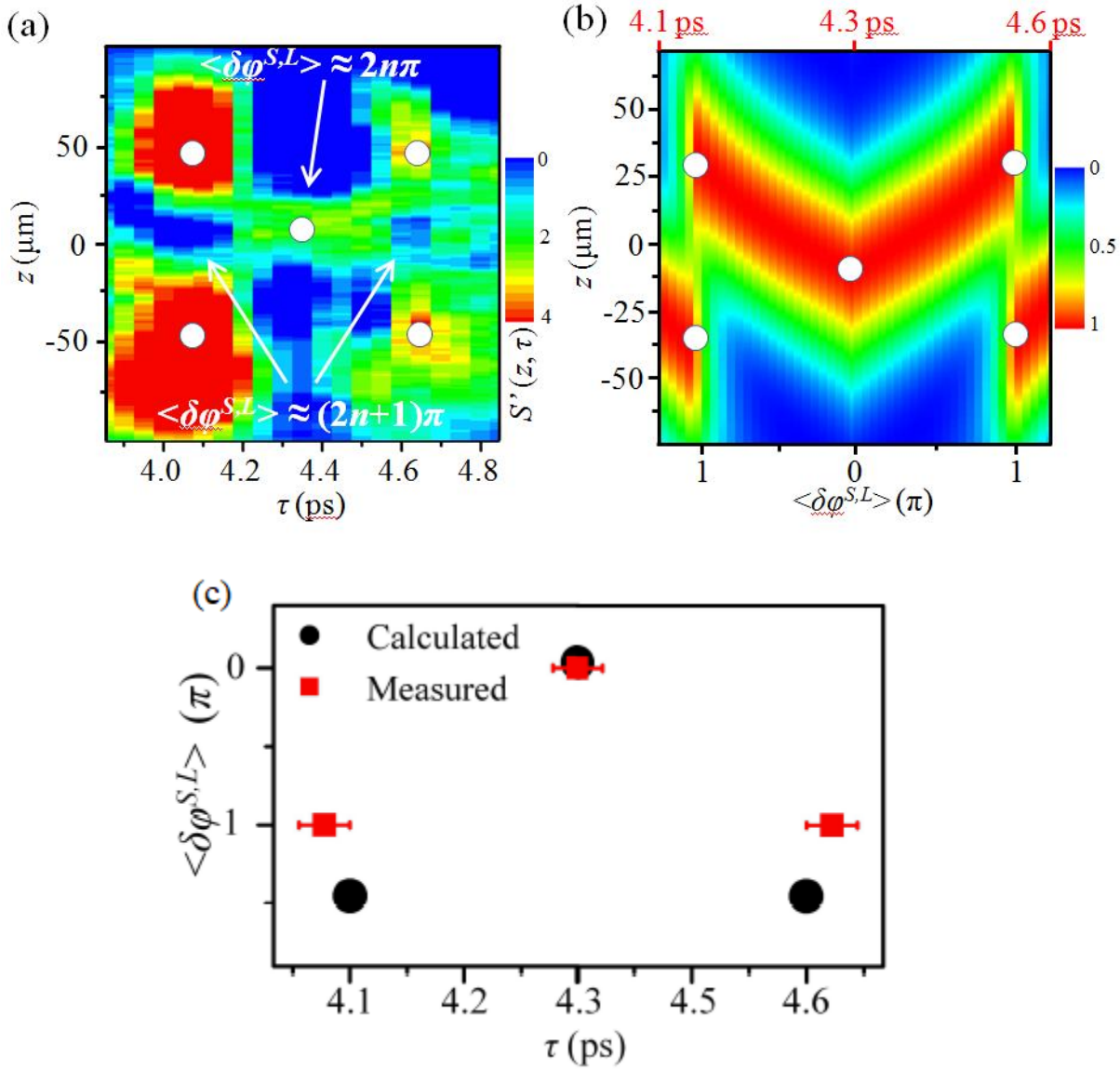

Figure 3.7 (a) Line outs of the Ar+ distribution at x = 0, y = 0, z around *Tr/2*. The corresponding calculated lines outs (normalized to unity) are shown in (b). The white lines in (a) and (b) show the peak of the distribution and the white circles the values that can be safely deduced by the experiment (c) Comparison between the measured (red–crossed triangles) and the calculated (black line) values of $\langle\delta\varphi^{S,L}\rangle$. For the measured values it was assumed that n = 1

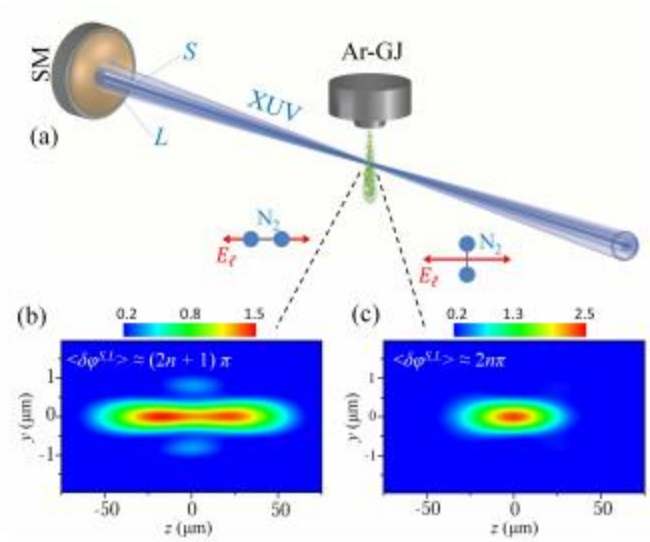

Figure 3.9 (a) Schematic illustration of the XUV focusing geometry used in the calculations.(b) and (c) Calculated XUV interference patterns around the focus for $\langle \delta\varphi^{S,L} \rangle \approx 2n\pi$ and $\langle \delta\varphi^{S,L} \rangle \approx (2n+1)\pi$, respectively.

3.4 Method used for the optimization of the aligning IR intensity pulse (pump pulse)

The degree of molecular alignment is proportional to the intensity of the aligning laser field (see section 1.3.2). However, a strong aligning pulse can lead to undesirable effects such as ionization of the molecules. High ionization rates lead lead to the formation of high plasma densities that influence the degree of alignment and the coherent properties of the emitted harmonics. This has a significant influence on the harmonic yield and the spatial distribution of the XUV beam. The former is associated with the phase mismatch (introduced by the plasma refractive index n_p) between the IR and the XUV radiation along the propagation axis in the HHG medium, while the later with the variation of n_p along the IR beam cross-section in the HHG area. The plasma presents a refractive index which depends on the radiation frequency as $n_p \approx 1 - \frac{{\omega_p}^2}{2\omega^2}$ (the approximation is valid due to the relatively low gas density used in HHG where it can be considered that $\omega_p << \omega$) where ω is the frequency of the driving laser field, $\omega_p = (\frac{e^2 N_e}{m_e \varepsilon_0})^{1/2}$ is the plasma frequency, N_e is the density of free electrons of electrons, m_e is the electron mass, e is the electron charge and ε_0 is the vacuum permittivity.

In the following we present experimental results depicting the usefulness of the IM on optimizing the molecular alignment conditions via measuring the wavefront distortion introduced in the XUV beam by the plasma. In order to do this we recorded pump-probe traces for higher intensities of the aligning pump laser pulse. In the following we present data recorded when the intensity of the pump beam increased by a

factor of 2 compared the intensities used in Fig. 3.3. Figure 3.10 shows the time evolution of the spatially integrated harmonic yield as a function of the delay τ for the two different pump intensity values $I_1^{pump} \approx 5\times10^{13}$ W/cm^2 and $I_2^{pump} \approx 1\times10^{14}$ W/cm^2 respectively. The probe pulse intensity is estimated to be $I^{probe} \approx 10^{14}$ W/cm^2 in both cases. For I_1^{pump} the harmonic yield depicts a modulation every $\tau \approx Tr/4$ as expected (figure 3.10 light grey line). The dominating effect is the creation of the molecular rotational wavepacket that evolves in time. The ionization level of the molecular ensemble and the corresponding plasma density can be considered as negligible. When the pump intensity was increased the situation is quite different (figure 3.10 black line). It is evident that I_2^{pump} the overall harmonic signal is reduced and the revival structure is distorted. As it is expected, the effect is more pronounced around the revival times $\tau \approx Tr/2$ and $\tau \approx Tr$ where the plasma density is increased due to the enchancment of the ionization rate (we note that the lifetime the plasma effect is in the ps time scale).

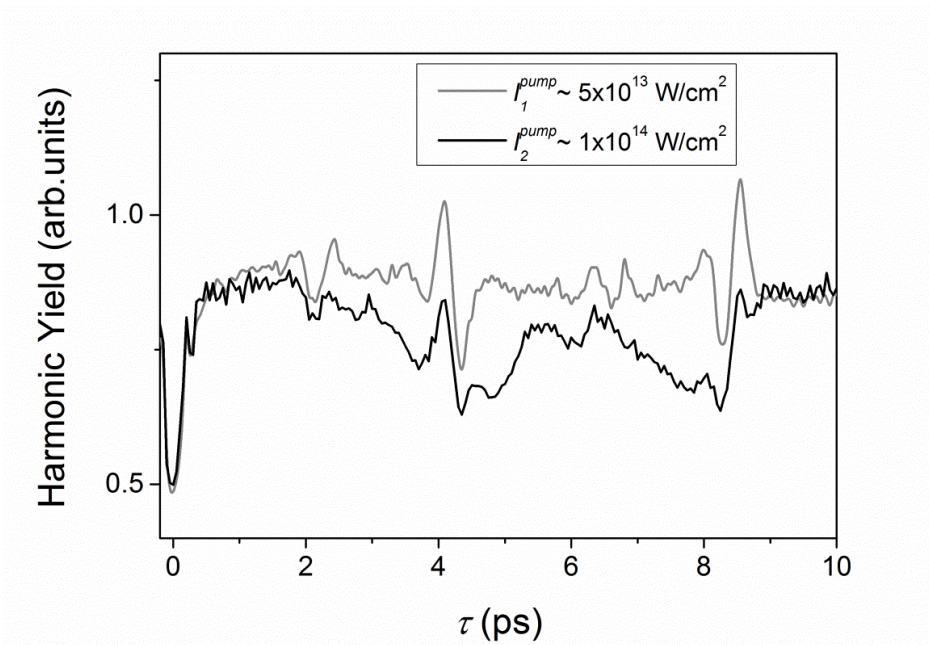

Figure 3.10: The time evolution of the spatially integrated harmonic yield for $I_1^{pump} \approx 5 \times 10^{13}\ W/cm^2$ (grey line) and $I_2^{pump} \approx 1 \times 10^{14}\ W/cm^2$ (black line).

The dependence of the spatial properties of the harmonics on the plasma generation is imprinted on the spatial intensity distribution at the far-field along the transverse *y* axis. Figure 3.11 illustrates the lineouts of the normalized Ar^+ distribution at $x = 0$, $z = 100$ μm, *y* (see figure 3.1b-left panel) as a function of τ for I_1^{pump} and I_2^{pump}. The lineout distribution for I_1^{pump}, is constant as depicted in figure 3.11a. On the contrary, for I_2^{pump} the distribution presents strong fluctuations along *y* axis (figure 3.11b). These

fluctuations of the spatial distribution are again more pronounced around $\tau \approx Tr/2$ and $\tau \approx Tr$ and originate variation of the refractive index along the IR beam cross section in the HHG medium i.e the peak intensity is higher at the center of the beam cross section then the tails. In particular, the laser beam presents a transverse intensity gradient. In terms of optical properties this translates to a gradient in the refractive index of the medium in the transverse directions *x* and *y* (z is the propagation direction). The gradient in the refractive index leads to deflection of the incoming beam IR beam and that leads to the wavefront distrortion of the emitted XUV radiation due to the spatial variation (associated to the change of the n_p) of the deflection of the incoming beam. According to Williams et al[93].

$$\varphi(x,y) = \int_0^L \nabla n_p(x,y,z)dz \tag{3.1}$$

where n_p is the plasma refractive index and L is the plasma length.

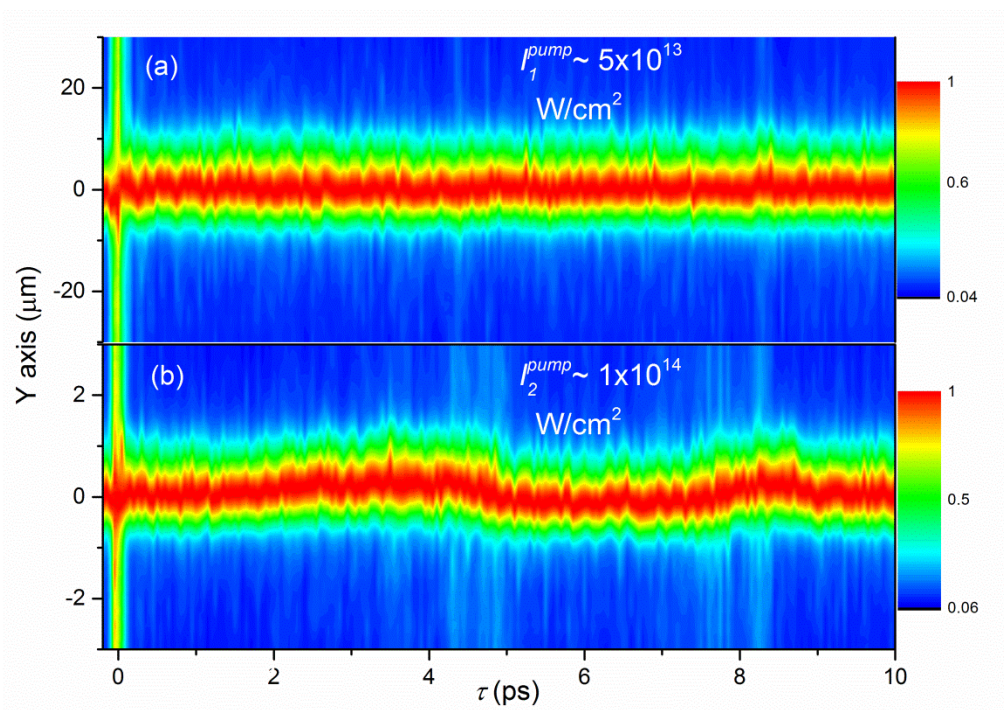

Figure 3.11: Contour plot showing the normalized lineouts along the *y* axis as a function of the delay for pump pulse intensity (a) $\approx 5 \times 10^{13}\ W/cm^2$ and (b) $\approx 1 \times 10^{14}\ W/cm^2$

A simplified schematic representation of the XUV wavefront distortion is illustrated in figure 3.12. The XUV focus position is unaffected by the refractive index gradient but the wavefront is distorted. This distortion is observed in the fluctuations of the spatial intensity distribution along y axis at the far field. The observed fluctuations of the lineout distribution are more pronounced around revival times because the plasma generation (and thus the gradient in the refractive index) is higher at these delays.

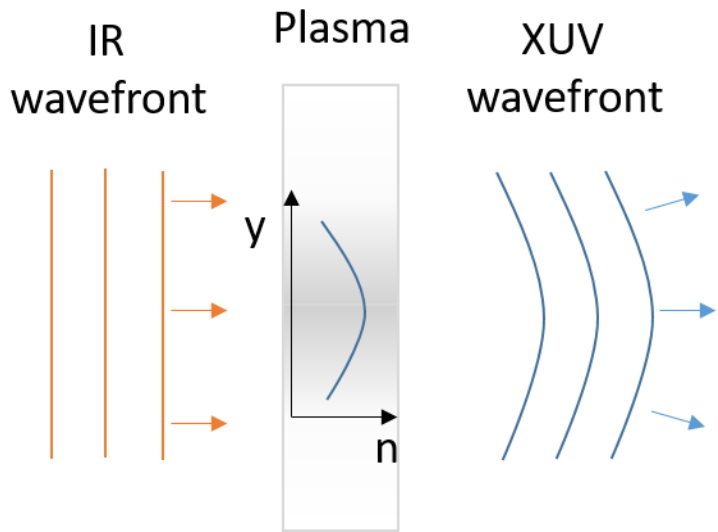

Figure 3.12: Schematic representation of the plasma gradient effect on the XUV beam wavefront. The plasma causes a gradient to the refractive index of the generation medium (inset panel). This gradient leads to wavefront distortion of the generated XUV radiation.

3.5 Conclusions

In this work, by utilizing a self-referenced approach we have measured electron quantum path interference effects in laser-driven aligned N_2 molecules and quantified their dependence on the orientation of the molecule. This approach overcomes a weakness in the majority of the demonstrated experimental approaches[25-28] which is the use of auxiliary references relaying on the assumption that they have similar response to strong field as the molecule under investigation. It is found that the phase difference between the S- and L- electron quantum paths is shifted by a value larger than π when the molecular axis is changing from parallel to perpendicular with respect to the polarization of the laser field. These findings, besides the fundamental interest on carrying out investigations on aligned diatomic molecules, in conjunction with longer wavelength-molecular-HHG schemes, can be used for the development of self-referenced attosecond spectroscopy approaches in a broad group of molecular species whose ionization potential is such that they may produce a broad harmonic spectrum[29,94.] Also, using the same approach we studied the impact of the plasma generation on the properties of the harmonic source. Specifically, it was shown that the plasma density distorts the alignment dynamics and has a strong contribution to the refractive index of the generating medium leading to the wavefront distortion of the harmonic radiation along the transverse plane.

Chapter 4

Polarization shaping of high-order harmonics in laser-aligned molecules.

4.1 Introduction

HHG from intense fs laser pulses provides experimental access to ultrafast dynamics and structure in atoms-molecules. In the majority of these studies the polarization of the harmonics is linear although there is a strong demand for HHG with high degree of ellipticity. In particular circularly polarized XUV radiation is very useful for the investigation of chirality sensitive light-matter interaction, circular dichroism, magnetic microscopy and ultrafast spin dynamics among others. Several theoretical approaches have been proposed for the generation of circularly polarized harmonics[95,96]. However, experimental demonstrations were still very limited until a couple of years ago and in all attempts the harmonic radiation was limited to low photon flux and/or poor ellipticity[51,97-98,100].

The past few years a number of experimental studies have been demonstrated that overcome these limitations. Fleischer et al.[100] in 2014 initiated this breakthrough where tunable polarization high harmonics generated using coplanar, elliptical polarized counter-rotating dichroic drivers. Kfir et al[101] using circularly polarized instead of elliptical counter rotating drivers measured the magnetic circular dichroism (MCD) in thin CO foil. Hickstein et al.[102] pushed further the concept of counter-rotating circularly-polarized laser pulses by showing that a non collinear geometry allows, among other advantages, the production of spatially separated circularly-polarized harmonics of the same frequency and opposite helicity. In the meantime, photoelectron circular dichroism of chiral molecules using elliptically-polarized light combined with a resonant interaction was reported by Ferré et al.[103] and elliptically-polarized XUV light produced by crossed polarized phase quadrature dichroic fields allowed the measurement of the MCD effect of nickel by Lambert et.al[104].

Here a different approach is demonstrated for circularly polarized HHG from circular polarized driven laser field using aligned molecules as a generating medium. This approach is based on a previous work of circularly polarized third harmonic generation (THG) from aligned CO_2 molecules[105]. Among other results the present application provides control of the polarization of the generated harmonics. The analytical model presented in ref.[105] was developed in the framework of the perturbation theory. The purpose of the present report is to demonstrate that aligned molecules can be used to produce high order harmonics with high degree of ellipticity in the strong field regime.

4.2 Experimental set up

The experiment is performed with the same laser system as the experiments presented in chapters 2&3. However, instead of an I-M the XUV radiation is detected with an XUV spectrometer. The experiment set up is presented in the figure 4.1 where the Ti:Sapphire laser system with a 10Hz repetition rate delivers ≈ 40 mJ pulses with duration ≈ 30fs centered at λ_0 = 800nm. The whole experimental set up is designed so as to be operated under vacuum conditions. The IR beam is split in two with a beam splitter in order to provide a sequence of an aligning and a generating pulse with an adjustable time delay. The aligning pulse is linearly polarized whereas the second pulse driving the harmonic process can be circularly polarized using a combination of a half-wave (HWP1) and a quarter-wave (λ/4) plate. For a better degree of alignment two BK7 thick glasses (total thickness of ≈ 2 cm) have been inserted to the aligning pulse arm in order to stretch the pulse. The two beams are focused by a 3-meter focal length and crossed at a small angle into a pulsed jet of CO_2 gas where the XUV radiations are generated. The intensity of the IR light on the spectrometer is reduced by a silicon wafer working with an incidence angle of 75°, i.e., close to the Brewster angle for 800 nm. The harmonic radiation is then reflected by a silver mirror, dispersed by an XUV spectrometer, and finally imaged on microchannel plates (MCP) detector. The back side of the MCP detector is mounted on a phosphor screen enabling recording the harmonic spectrum with a CCD camera. The harmonic radiation is then reflected by a silver mirror, dispersed by an XUV spectrometer, and finally imaged on microchannel plates (MCP) detector. The back side of the MCP detector is mounted on a phosphor screen enabling recording the harmonic spectrum with a CCD camera. The energy of the aligning pulse is estimated ~ 10 mJ with peak intensity $\sim 7 \times 10^{13} W/cm^2$ while that of the driving pulse is ~ 15 mJ with estimated peak intensity of $\sim 1 \times 10^{14} W/cm^2$

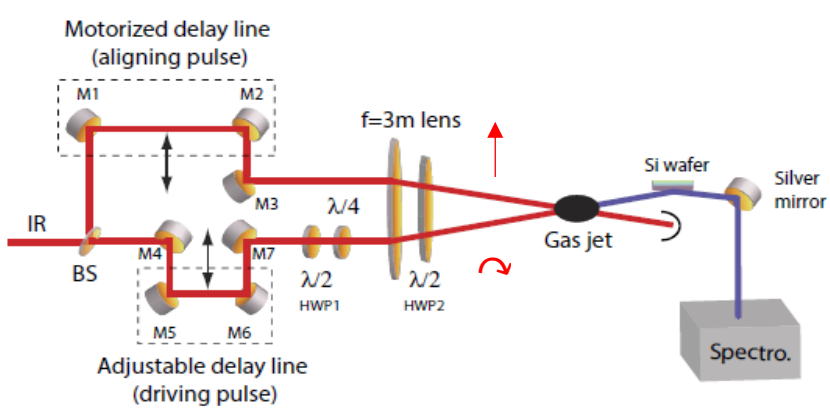

Figure 4.1: Experimental setup for polarization shaping of high-harmonic radiations generated in aligned molecules. M: Mirrors; BS: Beam splitter; HWP: Half-wave plates; λ/4: Quarter-wave plate.

4.3 Characterization of XUV analyzer

The polarization of the harmonics is measured thanks to the combination of polarization sensitive optical elements including the Si wafer, the silver mirror, and the grating of the spectrometer, the whole acting as an XUV reflective polarization analyzer favouring s-polarized waves. Since the HHG polarization measurements cannot be achieved by rotating the analyzer, the former is conducted by rotating both the aligning and the driving pulse around the optical axis using a large-aperture half-wave plate (HWP2) through which both pulses are passing.

Initially, the contrast of the analyzer has to be measured. The characterization of the XUV analyzer is performed by recording the XUV signal produced by unaligned molecules exposed to a linearly p-polarized pulse for various rotations of the HWP2. The ratio R of the detected XUV signal for the two perpendicular components of the linearly polarized field (i.e the s-polarized and the p-polarized fields) is the extinction ratio of the analyzer. For symmetry reasons the harmonics share the same symmetry with the driving field. Although all angular distributions presented in this work have been recorded by rotating the field to be analyzed with the aid of HWP2, for the sake of simplicity we will consider hereafter that the field is fixed whereas the analyzer is rotated.

Figure 4.2a (blue circles) depicts the signal of the 9th harmonic recorded over several turns of HWP2. The angle Φ describes the orientation of the analyzer axis, defined here as the direction along which its efficiency is maximum, with respect to the horizontal axis. The same signal depicted in a polar coordinates system is shown in Fig. 4.2b (blue circles). The extinction ratio R is ~ 4.5, much smaller than what is currently obtained with traditional polarizers.

An accurate determination of the contrast of the analyzer can be deduced from the modulation depth of the signal using a modified Malus' Law. The result of the simulation performed with the fitted contrast value R = 4.5 is shown for comparison in the same figures with the red line.

The two orthogonal components of the harmonic field polarized in the Oyz plane is written $\vec{E}(0, E_y, E_z)$ with

$$E_y = \left|E_y\right| e^{(i\varphi/2)} \tag{4.1}$$

$$E_z = \left|E_z\right| e^{(-i\varphi/2)} \tag{4.2}$$

where φ is the dephasing between the two components. The XUV polarization analyzer induces along both components a complex amplitude $a_y = \left|a_y\right| e^{i\psi_y}$ and $a_z = \left|a_z\right| e^{i\psi_z}$ respectively. The eventual dephasing introduced by the analyzer is $\psi = \psi_y - \psi_z$. The action of the analyzer is characterized by the tensor

$$\overrightarrow{\overrightarrow{A}} = \begin{pmatrix} 0 & 0 & 0 \\ 0 & a_p e^{i\psi_p} & 0 \\ 0 & 0 & a_s e^{i\psi_s} \end{pmatrix} \tag{4.3}$$

After the reflection of the analyzer the harmonic field is written as $E_a = \vec{A}.\vec{E}$. The dependence of its intensity with respect to the orientation of the analyzer is described by the Malu's law:

$$I_a(\Phi) = |a_p|^2 |E_y|^2 (\cos^2\Phi + R\sin^2\Phi) + |E_z|^2 (R\cos^2\Phi + \sin^2\Phi) + |E_y||E_z|(R-1)\sin 2\Phi \cos\varphi \quad (4.4)$$

where $R = (a_s/a_p)^2$ is the extinction ratio of the analyzer. The two amplitude components of the incident field can be obtained by measuring the signal for two orientations of the analyzer corresponding to $\Phi = 0$ and $\Phi = \pi/2$:

$$|E_y{}^2| \approx \frac{1}{(1+R)} \frac{I_a(\Phi=0) - RI_a(\Phi=\pi/2)}{I_a(\Phi=0) - I_a(\Phi=\pi/2)} \quad (4.5)$$

$$|E_z{}^2| \approx \frac{1}{(1+R)} \frac{I_a(\Phi=\pi/2) - RI_a(\Phi=0)}{I_a(\Phi=0) - I_a(\Phi=\pi/2)} \quad (4.6)$$

The IR field delivered by the laser system is initially polarized along the y-axis (i.e $|E_z| = 0$). Thus Equation 4.4 can take a simpler form for harmonics generated from a linearly polarized driving field. The red line in figure 4.2 is a fit using the simplified equation 4.4.

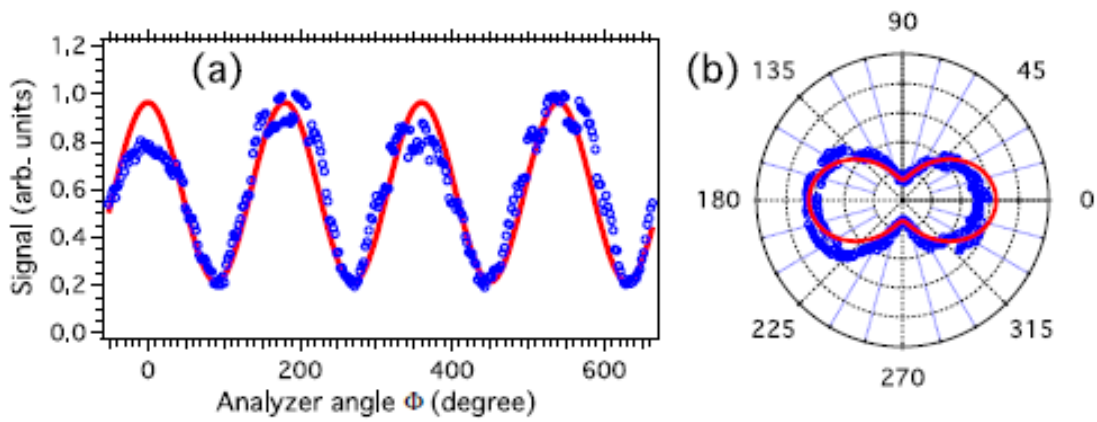

Figure 4.2: (a) Polarization analysis of the linearly polarized 9th harmonic at 88.9 nm. Each data point represents an averaging of 10 laser shots. (b) The same analysis depicted in a polar plot. With blue circles the experimental data and with red line the numerical calculation.

4.4 Experimental Results

HHG with elliptical polarization is allowed in a gas of aligned molecules if the polarization axis of the linear driving field is different with the molecular axis. The axial symmetry of the in this case is broken and a component of harmonic emission perpendicular to the one parallel to the laser polarization can be generated (see section 1.4). In order to increase the ellipticity of the harmonic emission, a circular driving field can be used. We should note here that the harmonic yield will be reduced in this case. Figure 4.3 depicts for instance the 9th harmonic generated by a circularly-polarized IR pulse in CO2 molecules for different temporal delays between the aligning and driving pulse. The alignment field is linearly polarized within the polarization plane of the driving field

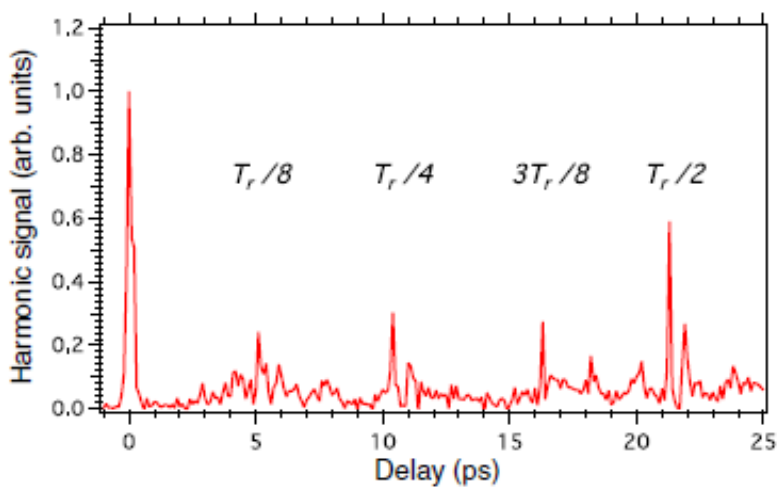

Figure 4.3: 9th harmonic versus delay between a linearly-polarized aligning and a circularly-polarized driving pulse**.** T_{rot} = 42.7 ps: full revival period of CO_2.

As a result of the anisotropy introduced by aligning the molecules, the harmonics generated by the circularly-polarized pulse should be elliptically polarized, the ellipticity of them being governed by the time delay between the alignment pulse and the driving field. In order to verify this assumption, both polarization components of the harmonic field produced from a circular polarized driving field must be resolved. Figure 4.4 (a) compares the harmonic signal recorded with two orthogonal orientations of the analyzer, namely vertical and horizontal. The difference between the two curves reveals that the polarization of the harmonic field varies with the delay as a result of the change occurring in the angular distribution of the molecules. In order to quantify the impact of this change, the polarization of the harmonic field is measured using the same methods as in Fig. 4.2. The result is shown in Fig. 4.4(b) for a delay set at 11.2 ps. Using the measured contrast value R the ratio of the two orthogonal harmonic components $r = |E_z|/|E_y|$, with E_y the field component along the horizontal y-axis and E_z along the vertical z-axis, and their phase difference can be

estimated (equation 4.4). The ratio is $r = 0.14$ and the dephasing $\varphi = 1.33$ rad. From the determination of r and φ the ellipticity ε of the XUV field can be estimated using the equation

$$\varepsilon = \tan(1/2\arcsin[\frac{2r}{(1+r^2)sin\varphi}]) \tag{4.7}$$

The ellipticity value at the delay 11.2 ps is 0.14. The small value of the ellipticity and the component ratio r reveals that the polarization of the EUV is close to linear with an orientation along the y-axis (i.e the p-wave is dominant). Because of the limited extinction ratio of the XUV analyzer, this small ellipticity produces a signal that is about 3 times larger [see Fig. 4.4(a)] when the axis of the analyzer is oriented along the horizontal direction of the field as compared to the vertical one. For comparison, an ideal analyzer would lead with the same field ellipticity to a contrast of about 50. The slight tilt of the angular distribution observed in the fitted curve of figure 4.2(b) is because of the small deviation of the dephasing φ from the expected value $\pi/2$. This small deviation remains within the experimental uncertainty.

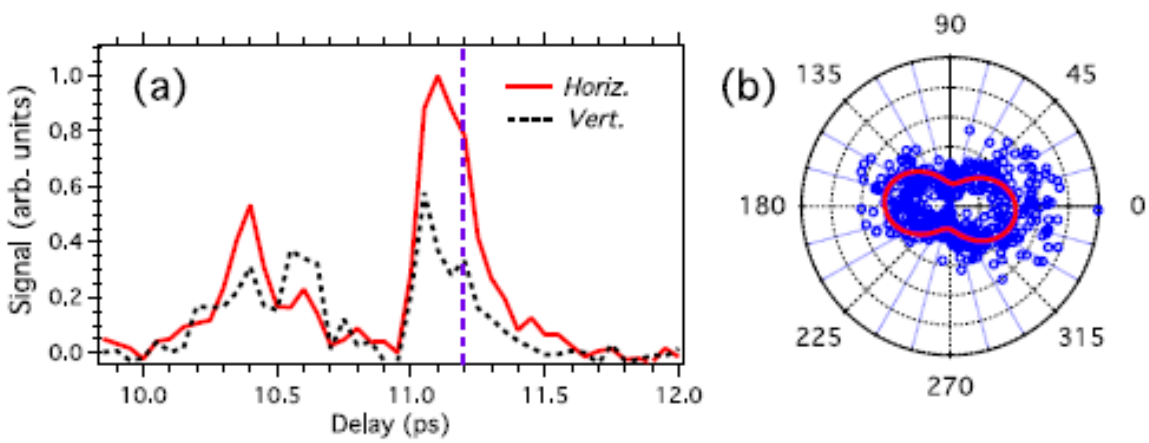

Figure 4.4: (a) 9th harmonic intensity recorded for the horizontal and vertical orientation of the analyzer axis. The dotted vertical line indicates the delay at which the polarization analysis is conducted (see right panel). (b) Polarization analysis with the experimental (numerical) data depicted with blue circles (red line). The fitted ellipticity is $\varepsilon = 0.14$.

As a general remark, it should be pointed out that ε provides an upper value of the ellipticity since our detection scheme does not allow to differentiate polarized from unpolarized light. Some unpolarized XUV component may be present due to the radial and temporal intensity variation of the lasers. However, due to the high nonlinearity of the harmonic generation process the most efficient generation results from the highest laser intensity part, where the intensity distribution does not vary significantly and thus the unpolarized XUV component remains small.

It is well known that the phase quadrature between the two oscillating field components is a first prerequisite in achieving a circular polarization. The second one is that the components should share the same amplitude. In principle, the latter can be obtained by adjusting the time delay so as to find a temporal domain where the two signals depicted in Fig. 4(a) are equal[105]. However, depending on the harmonic order and the degree of alignment, the two field components are not necessarily balanced when the harmonic amplitude is significant. To circumvent this problem, a small ellipticity is introduced along the horizontal or vertical direction of the driving field in order to increase the generation along the corresponding direction. This can be understood as analogous to the addition of a small linear component to a circularly-polarized IR field, the former producing harmonics preferentially along its direction. The ellipticity is introduced by slightly tilting the HWP1 from the direction of the optimum suppression of the harmonic signal. This approach is applied to the result presented in figure 4.5(a). The corresponding polarization analysis performed at a delay of 11.2 ps is shown in Fig. 4.5(b). The ellipticity and phase value derived from the least square fit are $\varepsilon = 0.85$ and $\varphi = 1.73$ rad, respectively. Although the amplitude ratio between the two field components is very close to unity ($r = 0.97$), the small difference between the fitted phase and $\pi/2$ (+ 9°) generates a small ellipticity of the theoretical curve. The polarization of Fig. 5(c) is obtained after a small shift of the delay, 11.18 ps and with a different adjustment of HWP1 so as to produce an elliptic polarization. Compared to the two previous cases, the major axis of the ellipse is now standing along the vertical direction, $r = 1.23$, with a phase $\varphi = 1.5$ rad (− 4°) that remains about constant, leading to an ellipticity $\varepsilon = 0.80$. The polarization shaping is also applicable for other harmonics. For instance, the result of Fig. 4.5(d) is obtained for the 7th harmonic with a delay of 10.45 ps. The adjusted ellipticity and phase are $\varepsilon = 0.74$ and $\varphi = 1.8$ rad (+ 13°), respectively. For technical reasons, it was not possible to measure both 7th and 9th harmonic simultaneously. The photon flux of the highly elliptical XUV beam just after the HHG medium is $4 \approx$ pJ, i.e 4×10^6 photons/pulse. This value is measured by means of a calibrated XUV photodiode in combination with the photoelectron spectra of a linear and circular XUV radiation (see section 4.5.)

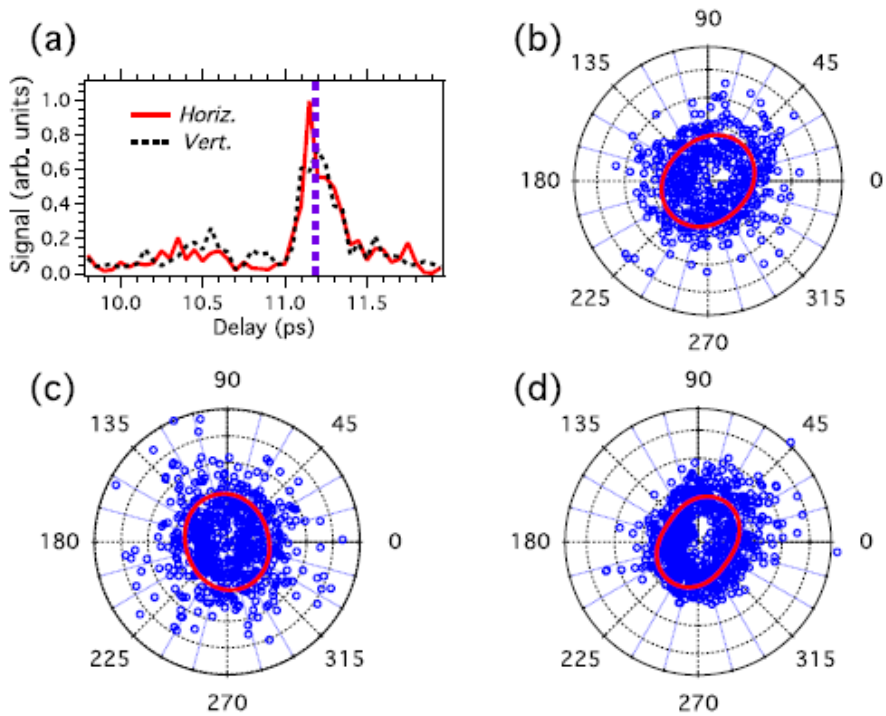

Figure 4.5: (a) Harmonic intensity recorded for the horizontal and vertical orientation of the analyzer axis. Harmonics generated with different polarizations states: (b) 9th harmonic at the delay 11.2 ps (ε = 0.85), (c) 9th harmonic at the delay 11.18 ps (ε = 0.8), and (d) 7th harmonic at the delay 10.45 (ε = 0.74).

4.5 XUV photon flux measurement

The energy of the circularly polarized 9th harmonic has been measured by means of a calibrated photodiode and a time-of-flight (TOF) photoelectron (PE) spectrometer, placed just after the photodiode. The energy of the high-order harmonics (XUV) generated using only the p-polarized probe IR beam has been measured with the calibrated XUV photodiode, placed after the silicon plate and a 150-nm-thick aluminum filter, which transmits harmonics with order q > 11th. This was done by moving the silver mirror (see Fig. 1) out of the harmonic beam path. The corresponding PE spectrum (S_{p-pol}^{PE}) induced by the interaction of the harmonics with order > 11th with argon atoms was recorded (black line in Fig .4.6) by moving the XUV photodiode out of the harmonic beam path. In this way the correspondence between the PE spectrum and the XUV energy has been established. A PE spectrum (S_{c-pol}^{PE}) has also been recorded (red line in figure 4.6) after the reduction of the 9th harmonic generated by the p-pol IR laser field to value (signal recorded from the XUV spectrometer) equal with the energy of the near circular 9th harmonic. This

measurement gives the correspondence between the S_{c-pol}^{PE} and the energy of the near circularly 9th harmonic.

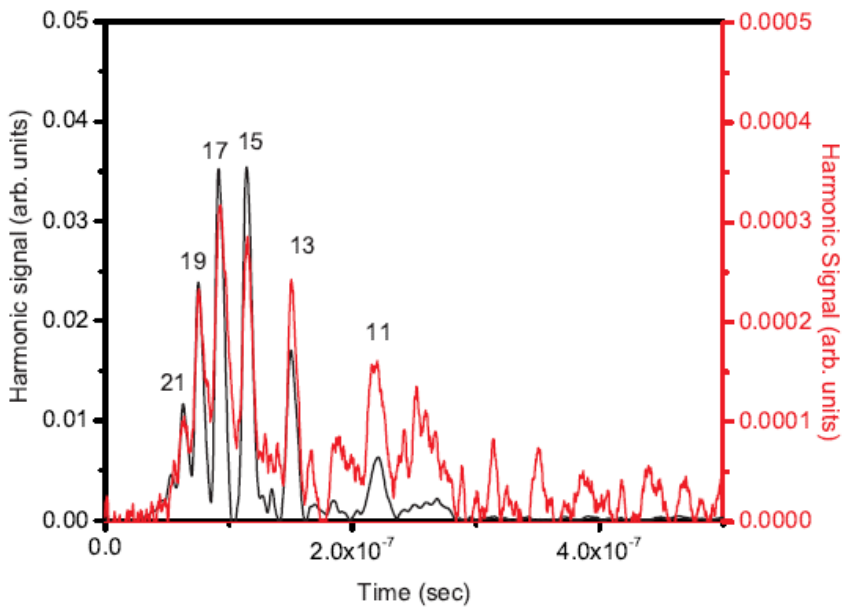

Figure 4.6: Photoelectron (PE) spectra resulted by the interaction of high-order harmonics with Ar (IP=15.76 eV). The black solid line shows the PE spectrum (S (PE) p-pol.) recorded in case of using only the p-polarized probe IR beam. In this case the energy of the XUV (EEUV) has been measured by means of a calibrated XUV photodiode. The red line shows the PE spectrum (S (PE) c-pol.) recorded in case of using a p-polarized probe beam which results to the generation of a p-polarized 9th harmonic with an energy approximately equal to the energy of the near-circularly polarized 9th harmonic.

With the above measurements the energy of the near-circularly polarized 9th harmonic just after the harmonic generation medium has been estimated by using the relation

$$E_{9th} = C_q \frac{E_{XUV}^{ph}}{QT_{Al}R_{si}} / \frac{S_{p-pol}^{PE}}{S_{c-pol}^{PE}} \tag{4.8}$$

with $Q(\approx 2)$, $T_{Al}(\approx 5)$, $R_{si}(\approx 0.6)$ and $C_q(\approx 0.2)$ being the quantum efficiency of the photodiode, the transmission of the Al filter, the reflectivity of the Si plate and $C_q = S_{p-pol}^{(9th)}/S_{p-pol}^{PE}$ (where $S_{p-pol}^{(9th)}$ is the PE signal of the 9th harmonic) respectively. In the above calculation it has been assumed that the energy of the 9th harmonic is approximately equal with the energy of the 11th, 13th harmonics, i.e $S_{p-pol}^{(9th)} = S_{p-pol}^{(11th,13th)}$. This approximation is valid since these harmonics are laying in the plateau region. The measured energy of the near circular EUV beam is $E_{9th} \approx 4$ pJ, i.e 4×10^6 photons/pulse.

4.6 Conclusions

We have shown that coherent short pulse XUV radiations with adjustable polarization state, ranging between linear and near circular, can be produced by molecular alignment assisted high-harmonic generation. The effect demonstrated here for high-order harmonics of low photon energies, which are suitable for probing molecular structures below their ionization thresholds, is in principle applicable to high-order harmonics of higher photon energies. The polarization shaping is based on the difference between the field vector components of the generated harmonic, whose relative amplitudes are ruled by the angular distribution of the molecules at the time they interact with a circularly-polarized driving field. Changing the delay between the aligning and driving pulse enables to modify to a large extent the amplitude ratio between the two field projections. In addition, the ability to generate circular polarization requires that the two electric field components are produced in phase quadrature. This condition is fulfilled in the case of third-harmonic generation where it has been shown experimentally and theoretically (in the framework of perturbation theory) that the transverse dipole components oscillate in phase quadrature. One might question whether this also applies to higher-order harmonics. Hereby it is revealed that the high-harmonic field components are in fact produced with the proper phase relation up to the 9th harmonic. It should be noticed that a small rotation of the polarization of the harmonics was reported for atoms driven by polarized light of moderate ellipticity ($0 < \varepsilon < 0.4$). In the present work, where the ellipticity of the driving field is one (or close to one) the amplitude of the two electric components of the fundamental field are comparable. Therefore, any dephasing occurring between the generated harmonic components, leading to a rotation of the harmonic field ellipse, would most probably result from the anisotropy of the potential of the aligned molecules rather than from the different amplitude of the two driving field components[106].

Compared to other existing techniques the present method, utilizing two external control parameters, namely the delay between the two pulses and the ellipticity (close to unity) of the driving XUV field, offers significant control over the polarization of the high-order harmonics generated by a non resonant single-color driving laser. In contrast to methods relying on the synchronisation of polarized femtosecond driving pulses[100,103,104] the polarization control mechanism investigated here does not require a stabilization of the relative phase between the two laser (aligning and driving) pulses with interferometric accuracy. It is also applicable to all the existing methods of producing isolated attosecond pulses with few or many cycle driving pulses and thus it can supply circularly polarized isolated pulses from the central part (highest intensity) of the driving laser pulse, assuming that the spectral components of the XUV continuum are generated with essentially the same ellipticity. While the question regarding the ellipticity variation in subsequent harmonics seeks for further experimental investigations, the ellipticity control of individual harmonics demonstrated here is important for applications in itself. Compared with recent techniques employing counter-rotating circularly-polarized femtosecond laser pulses reporting similar efficiency with

standard HHG process[100-,102], the moderate efficiency of the present method limits its application to high peak power lasers.

Chapter 5

Summary and outlook

In this work, strongly laser - driven aligned molecules have been used for the understanding the dynamics of molecular HHG and the generation of circular polarized pulses in the XUV spectral range. Towards these goals an approach with a combination of the Time Gated Ion Microscopy (I-M) technique with a pump-probe arrangement has been used.

Initially, Ion Microscope (I-M) has been used in HHG from atoms (Ar) where signatures of spatiotemporal coupling effects in HHG region have been measured. In particular, it was found that the short- and long-trajectory harmonics generated in gas phase media are focused in different positions in the detection area. This was measured by recording the of spatial ion distribution produced by single-XUV-photon ionization process at the XUV focus for different relative positions of the IR focus and the gas jet. Access to quantitative information which is connected to the divergence, the coherence properties and the photon flux of the harmonics has been obtained..

After measuring the spatiotemporal coupling effects taking place in the HHG region, we have developed a self-reference approach that provides access to the dynamics of HHG from aligned N_2 molecules by utilizing the pump-probe arrangement and the I-M. By spatially resolving the interference pattern produced by the spatiotemporal overlap of the harmonics emitted by the short– and long–electron quantum paths, we have succeeded in measuring in-situ their phase difference and disclose their dependence on molecular alignment. These findings, besides the fundamental interest on carrying out investigations in aligned diatomic molecules, in conjunction with longer wavelength–driven molecular–HHG schemes and coincidence detection arrangements, can be used for the development of self–referenced attosecond spectroscopy approaches and the recently demonstrated laser driven electron diffraction schemes.

In the last part of this work, the pump-probe arrangement has been used in order to generate circularly polarized XUV pulses using aligned molecules of CO_2 as a generating medium. This technique, utilizing two external parameters, the delay between the two pulses and the ellipticity of the driving IR field, offer significant control over the polarization of the XUV pulses generated by a single colour driving laser field. In contrast to methods relying on the synchronisation of polarized femtosecond driving pulses100 the present method does not require a stabilization of the relative phase between the two laser (aligning and driving) pulses with interferometric accuracy.

References

[1] T. Kanai , S. Minemoto and H. Sakai , "Quantum interference during high order harmonic generation from aligned molecules," Nature **435**, 470-474 (2005).

[2] M. Lein, "Molecular imaging using recolliding electrons," Journal of physics B: Atomic, molecular and optical physics**. 40 R:135**, (2007).

[3] M. Uiberacker, Th. Uphues, M. Schultze, A. J. Verhoef, V. Yakovlev, M. F. Kling, J. Rauschenberger, N. M. Kabachnik, H. Schröder, M. Lezius, K. L. Kompa, H.-G. Muller, M. J. J. Vrakking, S. Hendel, U. Kleineberg, U. Heinzmann, M. Drescher and F. Krausz, "Attosecond real-time observation of electron tunnelling in atoms," Nature **446**, 627 (2007).

[4] A. McPherson, G. Gibson, H. Jara, U. Johann, T. S. Luk, I. A. McIntyre, K. Boyer, and C. K. Rhodes, "Studies of multiphoton production of vacuum ultraviolet radiation in the rare gases," Journal of the Optical Society of America **B 4**, 595 (1987).

[5] P. B Corkum, "Plasma perspective on strong field multiphoton ionization," Physical Review Letters **71**, 1994 (1993).

[6] M. Lewenstein, Ph. Balcou, M. Yu. Ivanov, Anne L'Huillier, and P. B. Corkum, "Theory of high-harmonic generation by low-frequency laser fields," Phys. Rev. A **49**, 2117–2132 (1994).

[7] J. Itatani, J. Levesque , D. Zeidler ,H. Niikura, H. Pepin , J.C. Kieffer , P.B Corkum, and D.M Villeneuve. "Tomographic imaging of molecular orbitals," Nature **432**, 867–871 (2004).

[8] R. Velotta, N. Hay, M. B. Mason, M. Castillejo, and J. P. Marangos, "High-order harmonic generation in aligned molecules," Phys. Rev. Lett. **87**, 183901 (2001).

[9] M. Lein, N. Hay, R. Velotta, J. P. Marangos, and P. L. Knight, "Interference effects in high-order harmonic generation with molecules," Phys. Rev. A **66**, 023805 (2002).

[10] Lein M, Hay N, Velotta R, Marangos JP, and Knight PL. "Role of the intramolecular phase in high-harmonic generation," Phys. Rev. Lett. **88**, 183903 (2002).

[11] C. Vozzi, F. Calegari, E. Benedetti, J.-P. Caumes, G. Sansone, S. Stagira, and M. Nisoli, "Controlling two-center interference in molecular high harmonic generation," Phys. Rev. Lett. **95**, 153902–153904 (2005).

[12] R. Torres, N. Kajumba, J. G. Underwood, J. S. Robinson, S. Baker, J. W. G. Tisch, R. de Nalda, W. A. Bryan, R. Velotta, C. Altucci, I. C. E. Turcu, and J. P. Marangos, Phys. Rev. Lett. **98**, 203007 (2007).

[13] S. Baker, J. S. Robinson, C. A. Haworth, H. Teng, R. A. Smith, C. C. Chirila, M. Lein, J. W. G. Tisch, J. P. Marangos, Science **312**, 424 (2006).

[14] M. Meckel, A. Staudte, S. Patchkovskii, D. M. Villeneuve, P. B. Corkum, R. Drner, and M. Spanner, Nat. Phys. **10**, 594 (2014).

[15] E. Skantzakis, S. Chatziathanasiou, P. A. Carpeggiani, G. Sansone, A. Nayak, D. Gray, P. Tzallas, D. Charalambidis, E. Hertz, and O. Faucher, Sci. Rep. **6**, 39295 (2016)

[16] V. Loriot, P. Tzallas, E. P. Benis, E. Hertz, B. Lavorel, D. Charalambidis and O. Faucher, J. Phys. B **40**, 2503 (2007).

[17] W. Boutu, S. Haessler, H. Merdji, P. Breger, G. Waters, M. Stankiewicz, L. J. Frasinski, R. Ta¨Ieb, J. Caillat, A. Maquet, P. Monchicourt, B. Carr´e, and P. Sali`eres, Nat. Phys. 4, 545 (2008)

[18] S. Haessler, J. Caillat, W. Boutu, C. Giovanetti-Teixeira, T. Ruchon, T. Auguste, Z. Diveki, P. Breger, A. Maquet, B. Carr´e, R. Ta¨ıeb and P. Sali`eres, Nat. Phys. 6, 200-206 (2010).

[19] Y. Mairesse, N. Dudovich, D. Zeidler, M. Spanner, and D.M. Villenueve. "Phase sensitivity of high harmonic transient grating spectroscopy," Journal of Physics B: Atomic, Molecular, and Optical Physics, **43**:065401, 2010

[20] Y. Mairesse, D. Zeidler, N. Dudovich, M. Spanner, J. Levesque, D. M. Villeneuve, and P. B. Corkum. "High-order harmonic transient grating spectroscopy in a molecular jet," Phys. Rev. Lett. **100** (14):143903, 2008.

[21] A. Rupenyan, J. B. Bertrand, D. M. Villeneuve and H. J. Wörner, "All-Optical Measurement of High Harmonic Amplitudes and Phases in Aligned Molecules," Phys. Rev. Let. **108**, 033903 (2012).

[22] X. B. Zhou, R. Lock, W. Li, N. Wagner, M. M. Murnane, and H. C. Kapteyn, "Molecular recollision interferometry in high harmonic generation," Phys. Rev. Lett. **100**, 073902 (2008).

[23] R.M. Lock, X. B. Zhou, W. Li, M.M. Murnane, and H.C. Kapteyn, "Measuring the intensity and phase of high-order harmonic emission from aligned molecules," Chemical Physics **366**:22, 2009.

[24] O. Smirnova1, Y. Mairesse, S. Patchkovskii, N. Dudovich, D. Villeneuve , P.l Corkum and M. Y. Ivanov. "High harmonic interferometry of multi-electron dynamics in molecules," Nature **460**, 972–977 (2009).

[25] N. Wagner, X. Zhou, R. Lock, W. Li, A. Wuest, M. Murnane, and H. Kapteyn, "Extracting the phase of High order harmonic emission from a molecule using transient alignment in mixed samples," Phys. Rev. A **76**, 061403 (2007).

[26] T. Kanai, E. J. Takahashi, Y. Nabekawa, and K. Midorikawa, "Observing the attosecond dynamics of nuclear wavepackets in molecules by using high harmonic generation in mixed gases," Phys. Rev. A **77**, 041402 (2008).

[27] B. K. McFarland, J. P. Farrell, P. H. Bucksbaum, and M. Guhr, "High Harmonic Phase in Molecular Nitrogen," Phys. Rev. A **80**, 033412 (2009).

[28] J. B. Bertrand, H. J. Worner, P. Salieres, D. M. Villeneuve and P. B. Corkum, "Linked attosecond phase interferometry for molecular frame measurements," Nat. Phys. **9**, 174 (2013).

[29]A. Zaïr,T. Siegel,S .Sukiasyan,F. Risoud,L.Brugnera,C. Hutchison,Z. Divekib, T.Auguste, J.W.G.Tisch, P.Salières, M.Y.Ivanov,J. P.Marangos, "Molecular internal dynamics studied by quantum path interferences in high order harmonic generation," Chem. Phys. **414**, 184 (2013).

[30] M. Ferray, A.L'Huillier, X.F Li, L.A, Lompre, G. Mainfray, and C. Manus. "Multiple-harmonic conversion of 1064 nm radiation in rare gases," Phys. B: At. Mol. Opt. Phys. **21**, L31–5 (1988).

[31] A. Zaïr, M. Holler, A. Guandalini, F. Schapper, J. Biegert, L. Gallmann, U. Keller, A. S. Wyatt, A. Monmayrant, I. A. Walmsley, E. Cormier, T. Auguste, J. P. Caumes, and P. Salières, "Quantum Path Interferences in High-Order Harmonic Generation," Phys. Rev. Lett. **100**, 143902 (2008)

[32] C. Corsi, A. Pirri , E. Sali, A. Tortora , M. Bellini, "Direct interferometric measurement of the atomic dipole phase in high-order harmonic generation," Phys. Rev. Lett. **97**, 023901 (2006),

[33] J.E Kruse, P. Tzallas, E. Skantzakis, C. Kalpouzos, G. D. Tsakiris, and D. Charalambidis. "Inconsistencies between two attosecond pulse metrology methods: A comparative study, " Phys. Rev. A **82**, 021402 (2010)

[34] G. Kolliopoulos, B. Bergues, H. Schröder, P. A. Carpeggiani, L. Veisz, G. D. Tsakiris, D. Charalambidis, and P. Tzallas, "Revealing quantum path details in high-field physics," Phys. Rev. A. **90**, 013822 (2014).

[35] X. X. Zhou, X. M. Tong, Z. X. Zhao, and C. D. Lin, "Alignment dependence of high-order harmonic generation from N_2 and O_2 molecules in intense laser fields, " Phys. Rev. **A** 72, 033412 (2005).

[36] J. Itatani, D. Zeidler, J. Levesque, Michael Spanner, D. M. Villeneuve, and P. B. Corkum, "Controlling High Harmonic Generation with Molecular Wave Packets," Phys. Rev.Lett. **94**, 123902 (2005).

[37] X. M. Tong, Z. X. Zhao, and C. D. Lin, "Theory of molecular tunneling ionization," Phys. Rev. A **66,** 033402 (2002)

[38] B.K McFarland, J.P Fareel, P.H Bucksbaum and M.Ghur, "High harmonic generation from multiple orbitals in N_2," Science **322**, (2008)

[39] R. Torres R., R. De Nalda and J. Marangos, "Dynamics of laser-induced molecular alignment in the impulsive and adiabatic regimes:A direct comparison," Phys. Rev. A **72** , 023420 (2005)

[40] S. Fleischer, Y. Khodorkovsky, E. Gershnabel, Y. Prior, and I.S Averbukh, "Molecular alignment induced by ultrashort laser pulses and its impact on molecular motion", Isr. J. Chem. **52**, 414 (2012)

[41] H. Stapelfeldt. and T. Seideman, "Colloquim: Aligning molecules with strong laser pulses," Rev. of Mod. Phys. **75** (2003).

[42] Y. Ohshima and H. Hasegawa, " Coherent rotational excitation by intense non resonant laser fields," Int. Rev, in Phys. Chem. **29**, 619-663 (2010)

[43] Th. Vieillard, F. Chaussard, F. Billard, D. Sugny, O. Faucher, S. Ivanov, J.-M. Hartmann, C. Boulet, and B. Lavorel, "Field-free molecular alignment for probing collisional relaxation dynamics," Phys. Rev. A **87,** 023409 (2013)

[44] https://sites.google.com/site/drsebastienweber/programs/alignment-of-molecules

[45] WH Press, SA Teukolsky, WT Vetterling and BP Flannery, "Numerical recipes", Cambridge Univ. Press, New York (1992)

[46] I. V. Litvinyuk Kevin F. Lee, P. W. Dooley, D. M. Rayner, D. M. Villeneuve, and P. B. Corkum, "Alignment-Dependent Strong Field Ionization of Molecules," Phys. Rev. Lett. **90**, 233003 (2003).

[47] R. Torres R., R. De Nalda and J. Marangos, "Dynamics of laser-induced molecular alignment in the impulsive and adiabatic regimes:A direct comparison," Phys. Rev. A **72** , 023420 (2005)

[48] Seideman T. "Revival structure of aligned rotational wave packets," Phys. Rev. Lett. **83**, 4971– 4974 (1999).

[49] F. Rosca-Pruna and MJJ Vrakking, "Experimental observation of revival structures in picosecond laser-induced alignment of I_2," Phys. Rev. Lett. **87**, 153902 (2001).

[50] P. W. Dooley, I. V. Litvinyuk, Kevin F. Lee, D. M. Rayner, M. Spanner, D. M. Villeneuve and P. B. Corkum, "Direct imaging of rotational wave-packet dynamics of diatomic molecules," Phys. Rev. A **68**, 023406 (2003).

[51] X. Zhou, R. Lock, N. Wagner, W. Li, H.C. Kapteyn, and M.M. Murnane, "Elliptically Polarized HighOrder Harmonic Emission from Molecules in Linearly Polarized Laser Fields," Phys. Rev. Lett. **102**, 073902 (2009).

[52] V. Renard, M. Renard, S. Guérin, Y. T. Pashayan, B. Lavorel, O. Faucher, and H. R. Jauslin, "Postpulse molecular alignment measured by a weak field polarization technique," Phys. Rev. Lett. **90**, 153601 (4 pages) (2003).

[53] O. Faucher , B. Lavorel , E. Hertz, and F. Chaussard , "Progress in ultrafast intense laser science, " vii. pp. **79–108** (2011).

[54] G. Stavros, E. Harel, and S.R. Leone, "The influence of intense control laser pulses on homodyne detected rotational wave packet dynamics in O2 by degenerate four-wave mixing," J. Chem. Phys. **122**, 064301 (2005).

[55] S. Fleischer, I.S Averbukh, and Y. Prior , "Isotope-selective laser molecular alignment," Phys. Rev. A **74**, 041403(R) (2006).

[56] H. Hasegawa and Y. Ohshima , "Decoding the state distribution in a nonadiabatic rotational excitation by a nonresonant intense laser field," Phys. Rev. A **74**, 061401(R) (2006).

[57] R.O. Ghafur, K. Vidma, A. Gijsbertsen ,O.M Shir, T. Bäck , A. Meijer, W.J Van der Zande, D. Parker, and M.J.J Vrakking, "Evolutionary optimization of rotational population transfer," Phys. Rev. A **84**, 033415 (5 pages) (2011).

[58] P. Lambropoulos, "Mechanisms for Multiple Ionization of Atoms by Strong Pulsed Lasers," Phys. Rev. Lett. **55**, 2141–4 9 (1985).

[59] M Protopapas, C.H Keitel, and P.L Knight. "Atomic physics with super-high intensity lasers," Rep. Prog.Phys. **60**, 389–486 (1997).

[60] P. Agostini, F. Fabre, G. Mainfray, G. Petite, and N. K. Rahman , "Free-Free Transitions Following Six-Photon Ionization of Xenon Atoms," Phys. Rev. Lett. **42**, 1127–30 (1979).

[61] P. Kruit, J. Kimman, H. G. Muller, and M. J. Van der Wiel, "Electron spectra from multiphoton ionization of xenon at 1064, 532, and 355 nm," J Phys. Rev. A **28** 248–55 (1983).

[62] Yergeau F, Petite G and Agostini P J. Phys. B: At. Mol. Opt. Phys. **19**, L663–99 (1986)

[63] A. L'Huillier, L. Lompre , G. Mainfray, and C. Manus, "Multiply Charged Ions Formed by Multiphoton Absorption Processes in the Continuum," Phys. Rev. Lett. **48**, 1814–7 (1982).

[64] A. L'Huillier, L. Lompre , G. Mainfray and C. Manus, "Multiply charged ions induced by multiphoton absorption in rare gases at 0.53 μm," Phys. Rev. A **27**, 2503–12 (1983).

[65] B. Walker, E. Mevel, B. Yang, P. Breger, J. Chambaret, A. Antonetti , L. Dimauro and P. Agostini, "Double Ionization in the Perturbative and Tunneling Regime," Phys. Rev. A **48,** R894–7 (1993)

[66] P. Tzallas, D. Charalambidis, N. A. Papadogiannis, K. Witte, and G. D. Tsakiris, "Direct observation of attosecond light bunching," Nature **426**, 267–71 (2003).

[67] P. Tzallas, D. Charalambidis, N. A. Papadogiannis, K. Witte, and G. D. Tsakiris, " Second-order autocorellation of attosecond XUV pulse trains," J. Mod. Opt. **52**, 321–40 (2005).

[68] P. Hansch, M. A. Walker, and L. D. Van Woerkom, "Spatially dependent multiphoton multiple ionization," Phys. Rev. A **54**, R2559 (1996).

[69] M. A. Walker, P. Hansch, and L. D. Van Woerkom. "Intensity-resolved multiphoton ionization: Circumventing spatial averaging," Phys. Rev. A **57**, R701 (1998).

[70] B. Witzel, C.J. Uiterwaal, H. Schröder, D. Charalambidis and K-.L Kompa, "Analysis of multiphoton ionization of metal atoms in the saturation regime using subpicosecond KrF laser pulses," Phys. Rev. A **58**, 3836–48 (1998).

[71] M.Wagner and H. Schroder. "A novel four grid ion reflector for saturation of laser multiphoton ionization yields in a time of flight mass spectrometer," Int. J. Mass Spectrom. Ion Processes **128**, 31–45 (1993).

[72] M Schultze, B. Bergues, H. Schröder, F. Krausz and K-L Kompa, "Spatially resolved measurement of ionization yields in the focus of an intense laser pulse," New J. Phys**. 13**, 033001 (2011).

[73] N. Tsatrafyllis, B. Bergues, H. Schröder, L. Veisz, E. Skantzakis, D. Gray, B. Bodi, S. Kuhn, G. D. Tsakiris, D. Charalambidis and P. Tzallas, "The ion microscope as a tool for quantitative measurements in the extreme ultraviolet," Sci. Rep. **6**, 21556 (2016).

[74] M. Bellini, C. Lynga , A. Tozzi ,M.B Gaarde, T.W Hansch, A. L'Huillier and C.G Wahlström, "Temporal Coherence of Ultra Short Harmonic Pulses," Phys. Rev. Lett. **81**, 297 (1998).

[75] Y. Mairesse, A. de Bohan, L. J. Frasinski, H. Merdji, L. C. Dinu, P. Monchicourt, P. Breger,M.Kovacev, R. Taieb, B. Carr´e, H. G. Muller, P. Agostini, and P. Salieres, "Attosecond synchronization of high-harmonic soft x-rays," Science 302, 1540 (2003).

[76] P. Salieres, T. Ditmire, M.D Perry, A. L'Huillier, and M. Lewenstein, "Angular distributions of high-order harmonics generated by a femtosecond laser," J. Phys. B: At. Mol. Opt. Phys. **29**, 4771–4786 (1996)

[77] C.-G. Wahlström, J. Larsson, A. Persson, T. Starczewski, S. Svanberg, P. Salières, Ph. Balcou, and Anne L'Huillier, "High-order harmonic generation in rare gases with an intense short-pulse laser," Phys. Rev. A **48**, 4709 (1993).

[78] Xinkui He, M. Miranda,J. Schwenke, O. Guilbaud,T. Ruchon,C. Heyl, E. Georgadiou, R. Rakowski, A. Persson, M. B. Gaarde, and A. L'Huillier, "Spatial and spectral properties of the high-order harmonic emission in argon for seeding applications," Phys. Rev. A **79**, 063829 (2009)

[79] J.E Kruse, P. Tzallas, E. Skantzakis, C. Kalpouzos, G. D. Tsakiris, and D. Charalambidis. "Inconsistencies between two attosecond pulse metrology methods: A comparative study, " Phys. Rev. A 82, 021402 (2010)

[80] T. Auguste, P. Salières, A. S. Wyatt, A. Monmayrant, I. A. Walmsley, E. Cormier, A. Zaïr, M. Holler, A. Guandalini, F. Schapper, J. Biegert, L. Gallmann, and U. Keller, "Theoretical and experimental analysis of quantum path interferences in high-order harmonic generation," Phys. Rev. A **80**, 033817 (2009)

[81] C. J. Lai and F. X. Kärtner, "The influence of plasma defocusing in high harmonic generation," Optics Express **19**(23), 22377-22387 (2011).

[82] M. B. Gaarde, J. L. Tate, and K. J. Schafer, "Macroscopic aspects of attosecond pulse generation," J. Phys. B: At. Mol. Opt. Phys. **41**, 132001 (2008)

[83] P. Antoine, A. L'Huillier, and M. Lewenstein, "Attosecond Pulse Trains Using High–Order Harmonics," Phys. Rev. Lett. **77**, 1234 (1996).

[84] Anh–Thu Le, R. R Lucchese, and C.D. Lin, "Uncovering multiple orbitals influence in high harmonic generation from aligned N_2," J. Phys. B **42**, 211001 (2009).

[85] Z. X. Zhao, X. M. Tong, and C.D. Lin, "Alignment-dependent ionization probability of molecules in a double-pulse laser field," Phys. Rev. A **67**, 043404 (2003).

[86] T. K. Kjeldsen, and L. B. Madsen, "Strong-field ionization of N_2: length and velocity gauge strong-field approximation and tunnelling theory," J. Phys. B **37**, 2033 (2004).

[87] C. B. Madsen and L. B. Madsen, "High-order harmonic generation from arbitrarily oriented diatomic molecules including nuclear motion and field-free alignment," Phys. Rev. A **74**, 023403 (2006).

[88] Y. Mairesse, J. Levesque, N. Dudovich, P.B Corkum, and D.M Villeneuve, "High harmonic generation from aligned molecules–amplitude and polarization," J. Mod. Opt. **55**, 2591 (2008).

[89] J. Muth–Bohm , A. Becker, and F. H. M. Faisal, "Suppressed Molecular Ionization for a Class of Diatomics in Intense Femtosecond Laser Fields," Phys. Rev. Lett. **85**, 2280 (2000)

[90] H. Wikmark, C. Guo, J. Vogelsang, P. W. Smorenburg, H. Coudert-Alteirac, J. Lahl, J. Peschel, P. Rudawski, H. Dacasa, S. Carlström, S. Maclot, M. B. Gaarde, P. Johnsson, C. L. Arnold, and A. L'Huillier "Spatiotemporal coupling of attosecond pulses," PNAS **116**, 4779 (2019).

[91] S. Chatziathanasiou, S. Kahaly, D. Charalambidis, P. tzallas and E. Skantzakis, Opt. Express., "Imaging the source of high-harmonics generated in atomic gas media," Opt. Express **27**, 9733 (2019).

[92] M. Born and E. Wolf, Principles of Optics (Pergamon, New York, 1968)

[93] G.O Williams, H.-K Chung, , S.M Vinko, S. Künzel, A.B. Sardinha, , Ph. Zeitoun, M. Fajardo "Method of time resolved refractive index measurements of X-ray laser heated solid," Phys. Plasmas **20**, 042701 (2013).

[94] R. Torres, T. Siegel, L. Brugnera, I. Procino, J. G. Underwood, C. Altucci, R. Velotta, E. Springate, C. Froud, I. C. E. Turcu, M. Yu. Ivanov, O. Smirnova, and J. P. Marangos, "Extension of high harmonic spectroscopy in molecules by a 1300 nm laser field," Opt. Expr. **18**, 3174 (2010).

[95] K.-J. Yuan, and A. D Bandrauk. "Circularly polarized molecular high-order harmonic generation in H2+ with intense laser pulses and static fields," Phys. Rev. A **83,** 063422 (2011).

[96] D. B. Milošević, W. Becker and R. Kopold,. "Generation of circularly polarized high-order harmonics by two-color coplanar field mixing," Phys. Rev. A **61,** 063403 (2000).

[97] X.-M. Tong and S.-I Chu. "Generation of circularly polarized multiple high-order harmonic emission from two-color crossed laser beams," Phys. Rev. A **58,** R2656–R2659 (1998).

[98] Y. Mairesse, J. Higuet, N. Dudovich, D. Shafir, B. Fabre, E. Mével, E. Constant, S. Patchkovskii, Z. Walters, M. Yu. Ivanov, and O. Smirnova. "High harmonic spectroscopy of multichannel dynamics in strong-field ionization,". Phys. Rev. Lett. **104,** 213601 (2010).

[99] B. Vodungbo, A. B. Sardinha, J. Gautier, G. Lambert, C. Valentin, M. Lozano, G. Iaquaniello, F.Delmotte, S.Sebban, J. Lüning, and P. Zeitoun. "Polarization control of high order harmonics in the EUV photon energy range," Opt. Express **19,** 4346–4356 (2011).

[100]A. Fleischer, O. Kfir, T. Diskin, P.Sidorenko and O. Cohen. "Spin angular momentum and tunable polarization in high-harmonic generation," Nature Photon. **8,** 543–549 (2014).

[101] O. Kfir, P. Grychtol, E. Turgut, R. Knut, D. Zusin, D. Popmintchev, T. Popmintchev, H. Nembach, J. M. Shaw, A. Fleischer, H. Kapteyn, M. Murnane and O. Cohen. "Generation of bright phase-matched circularly-polarized extreme ultraviolet high harmonics," Nature Photon. **9,** 99–105 (2015).

[102] D. D. Hickstein, F. J. Dollar, P. Grychtol, J. L. Ellis, R. Knut, C. Hernández-García, D. Zusin, C. Gentry, J. M. Shaw, T. Fan, K. M. Dorney, A. Becker, A. Jaroń-Becker, H. C. Kapteyn, M. M. Murnane and C. G. Durfee. "Non-collinear generation of angularly isolated circularly polarized high harmonics," Nature Photon. **9,** 743–750 (2015).

[103] A. Ferré, C. Handschin , M. Dumergue , F. Burgy , A. Comby , D. Descamps , B. Fabre , G. A. Garcia , R. Géneaux , L. Merceron , E. Mével , L. Nahon , S. Petit , D. Staedter , S. J. Weber , T. Ruchon, B. Pons , V. Blanchet , Y. Mairesse . "A table-top ultrashort light source in the extreme ultraviolet for circular dichroism experiments," Nature Photon. **9**, 93–98 (2015).

[104] G. Lambert, B. Vodungbo, J. Gautier, B. Mahieu, V. Malka, S. Sebban, P. Zeitoun, J. Luning, J. Perron, A. Andreev, S. Stremoukhov, F. Ardana-Lamas, A. Dax, C. P. Hauri, A. Sardinha and M. Fajardo. "Towards enabling femtosecond helicity-dependent spectroscopy with high-harmonic sources," Nat. Commun. **6**, 1–6 (2015).

[105] J. Houzet, E. Hertz, F. Billard, B. Lavorel, and O. Faucher. "Molecular alignment allows low-order harmonic generation by circular light in a gas," Phys. Rev. A **88**, 023859 (2013).

[106] P. Antoine, B. Carré, A. L'Huillier and M. Lewenstein. "Polarization of high-order harmonics," Phys. Rev. A **55,** 1314–1324 (1997).